Contents

A STUDY OF THE REACTION $\pi^- p \rightarrow \eta n$ IN THE REGION OF THE N*(1688)

Roger Burton Chaffee

Lawrence Berkeley Laboratory
University of California
Berkeley, California

ABSTRACT

In an experiment performed at the Bevatron, a negative-pion beam incident on a 20-cm liquid-hydrogen target produced reactions of the form $\pi^- p \rightarrow$ neutral final state. The final-state neutron was detected by plastic-scintillator counters. The final-state photons were detected by lead-plate spark chambers, which covered about 3.7π solid angle, or by lead-scintillator sandwich counters, which covered most of the open face of the spark-chamber array.

For this analysis, a kinematic fit was done on the L.B.L. computer for each event in which two photons were detected. For each momentum, events which fit the hypothesis $\pi^- p \rightarrow \eta n$ were binned according to the calculated production cosine, and the resulting distributions were corrected by comparing to the results of a Monte-Carlo calculation for the same reaction. The differential cross-section was calculated for each bin, and the values for each momentum were fit to a sum of Legendre polynomials in production cosine.

In the final chapter of this thesis, the Legendre polynomial coefficients, the total cross-section, and the differential cross-sections extrapolated to 0° and 180° are compared to the results of other experiments, and some speculations are offered as to the spin-parity states which affect the measured behavior of the reaction. The conclusion is drawn that the N (1688) does not contribute, but that the N (1670) does, with a cross-section of (0.84±0.21) mb.

I. INTRODUCTION

A. Eta Mesons

The eta meson was first detected experimentally[1] in the reaction

$$\pi^+ d \rightarrow p_s p \pi^+ \pi^- \pi^o$$

where it appeared as a peak in the mass spectrum of the three-pion system. The peak is due to the presence of the reaction

$$\pi^+ d \rightarrow p_s p \eta$$

and decay

$$\eta \rightarrow \pi^+ \pi^- \pi^o$$

in which the total mass of the three-pion system must be the mass of the eta.

The eta was later observed[2] in the reaction

$$\pi^- p \rightarrow \eta n \qquad (1)$$

and subsequent decay

$$\eta \rightarrow \gamma\gamma \qquad (2)$$

which definitely established its quantum numbers as $J^P I^G = 0^+ 0^-$.

The mass of the eta is (548.8±0.6) MeV.[3] The width is (2.63±0.58) KeV,[3] corresponding to a lifetime of 2.05×10^{-19} sec.

E. Eta Production

1. General

The reaction

$$\pi^- p \rightarrow \eta n \qquad (1)$$

is particularly interesting to study. The relative simplicity of the two-body final state leads theorists to the hope of analyzing the dynamics of the reaction, without becoming embroiled in the kinematics of many-body states. ["Kinematics", roughly speaking, is any part of a particle interaction that is understood in principle, although it is generally too complex to be solved in any particular case. "Dynamics" is what is left, and is not understood even in principle.]

The reaction is a member of the family of interactions of pseudoscalar mesons with spin-1/2 baryons, and of the isospin 1/2 side of the family. It is therefore a close relative of the isospin 1/2 part of the pion-nucleon scattering reactions

$$\pi^- p \rightarrow \pi^- p \qquad (3)$$

and

$$\pi^- p \rightarrow \pi^0 n \qquad (4)$$

Both of these have been studied extensively, for reasons of experimental simplicity. Analogy with pion-nucleon scattering is an aid in the analysis of eta production. In turn, the eta-neutron state is purely isospin 1/2, and can provide information about the isospin 1/2 part of the pion-nucleon interaction, without the need for separating out the isospin 3/2

part.

In particular, analysis of the pion-nucleon reaction has shown resonance behavior. Around the energy region of this experiment, say from eta-neutron threshhold at 1488 MeV up to around 1900 MeV center-of-mass energy, pion nucleon scattering is strongly influenced by the production and subsequent decay of intermediate particles, in reactions of the form

$$\pi N \rightarrow X \rightarrow \pi N$$

The eta-nucleon final state has the same quantum numbers, and must couple to the same resonances, in reactions of the form

$$\pi N \rightarrow X \rightarrow \eta N$$

although the coupling of the intermediate particle to the two channels may be very different. Since each intermediate particle has a definite spin and parity, its presence at a particular energy is signalled by the behavior of the differential cross-section as a function of scattering angle. Only relatively crude statements about the intermediate states can be made from measurements of the total cross-section. Detailed analysis of the differential cross-section for eta production, with an expansion in terms of Legendre polynomials, should show the presence of some of the same intermediate resonances as are found in the isospin 1/2 channel of pion-nucleon scattering, and may reveal other intermediate particles which are coupled relatively weakly to the pion-nucleon channel.

2. Parameterization of Experimental Results

The total cross-section for the reaction (1) measures only the probability that the reaction will occur, with no reference to the directions of motion of the particles. The total cross-section is a function of the relative motion of the beam and target particles, and can be expressed as a function of the beam momentum, beam energy, barycentric momentum, or total (barycentric) energy. In discussing resonance behavior and other theories of the interactions involved, total energy is often the most appropriate parameter. However, one finds that most experiments are done in the laboratory system, with a beam and a target, and the measured variable is the beam momentum. For this reason, this thesis generally refers to beam momentum, in MeV/c, and the total energy is given in parentheses.

Differential cross-section is a function of both relative motion and direction. The usual angular variable is the cosine of the barycentric scattering angle. It is difficult to display this function of two variables in a fashion which compares the results of measurements at different energies. The usual method is to fit the cross-section measurement at each energy as a sum of Legendre polynomials,

$$\frac{d\sigma}{d\Omega} = \lambda^2 \sum_{\ell=0}^{\ell_{max}} A_\ell P_\ell(\cos\theta)$$

where λ is the reciprocal momentum of the incident

pion in the c.m. system, A_ℓ are the adjustable parameters, θ is the scattering or production angle in the c.m. system, and P_ℓ are the Legendre polynomials. The choice of the maximum order for the fit is often made on less than rigorous grounds. Eulos et al.[3] are typical:

> "First,...we have elected to have the maximum value of ℓ always even....The last coefficient is sometimes consistent with zero....Secondly,...that value of ℓ_{max} was chosen where the χ^2 probability had clearly reached its asymptotic value as a function of ℓ_{max}. Furthermore, the value of ℓ_{max} was never allowed to decrease at momenta above where it was first needed."

In this respect, expansion in terms of Legendre polynomials is considerably better than expansion in a power series, because the legendre polynomials are orthogonal in the range -1 to +1, and the inclusion of another term in the fit generally doesn't significantly affect the coefficients of lower-order terms. The value of ℓ_{max} is significant if one chooses to describe the interaction as composed of a sum of different amplitudes, each of definite angular momentum. Higher angular momentum states require higher-order terms in the fit to the differential cross-section, and, conversely, the success of a low-order fit limits the number of amplitudes which can be contributing in the model.

3. The Experimental Situation

By 1969, several experimental groups[4-8] had measured total and differential cross-sections for the reaction (1). Most published results concerned the behavior of the cross-section in the energy region just above threshhold, and the conclusion had been reached that the differential cross-section in this region is isotropic, and that the total cross-section rises linearly with the barycentric momentum of the final state. Both effects indicate that, close to threshhold, eta production is purely S-wave. This is in agreement with phase-shift analysis of pion-nucleon scattering, which shows the existance of an S_{11} resonance with a mass of 1500 to 1600 MeV.[9-12]

At higher energies, the situation was less clear. Richards et al.[4] used steel-plate spark chambers to detect the photons resulting from the two-photon decay of the eta. They did not attempt to detect the neutron. They measured and fit to a sum of Legendre polynomials the distribution of directions of the bisector of the two photon directions. The final distribution of eta directions was made by a mathematical transformation on the fit to the bisector distribution, and depended in part on the fact that their spark chambers covered the entire solid angle. They found that terms through P_2 were needed at c.m. energies as low as 780 MeV/c (1545 MeV), and that terms in P_3 were needed above 1005 MeV/c (1675 MeV).

However, their fits did not require a term in P_4 until their highest energy, at 1440 MeV/c (1900 MeV).

Bulos et al.[5] used a similar experimental scheme, with an array of steel-plate spark chambers which covered approximately 2/3 of the total solid angle. Because their angular coverage was incomplete, they used Monte-Carlo methods to derive the distribution of eta directions from the observed bisector distribution. Their final publication on the subject agreed that terms in P_2 were needed at the energies indicated by Richards et al, but they found P_3 and P_4 terms necessary at 860 MeV/c (1595 MeV) and above.

In the region above 875 MeV/c (1600 MeV), no other experiments had measured differential cross-section in the entire range of production cosine. The neutron detectors of Deinet et al.[7] were not positioned to cover the entire range of neutron laboratory angles which were kinematically allowed at their higher energies. The points that they did measure were in agreement with the above experiments.

4. Phase-Shift Analyses

Several papers[8-12] have been published giving the results of phase-shift analyses of the available data for reaction (1). The fits generally allow resonant behavior in several spin-parity states, with masses and widths which may vary or may be fixed at values found in pion-nucleon scattering. Models for background terms may allow only kinematic factors, or they may suppose t-channel exchanges. The disparate assumptions and results emphasize the need for more numerous and more accurate measurements of the differential cross-section in the entire angular range, and of polarization parameters.

II. EXPERIMENTAL PROCEDURE AND EQUIPMENT

A. General

The experimental apparatus was designed to collect information about the reactions

$$\pi^- p \rightarrow \text{All Neutrals}$$

The equipment consisted of a beam transport system, to direct negative pions from the Bevatron to the target, a liquid hydrogen target, neutron detectors, and lead-plate spark chambers in which the photons would convert and leave detectable tracks. In the beam line were counters to detect the incoming beam particles, and surrounding the liquid hydrogen target were counters to veto interactions with charged products. The counters were monitored and the spark chambers triggered by an electronic logic system.

Tracks in the chambers were photographed, along with an array of flash lamps with coded information from the counters. The information for each recorded event went on one frame of 35-mm film.

A diagram of the apparatus is shown in Fig. 1. A more complete description of the individual parts follows.

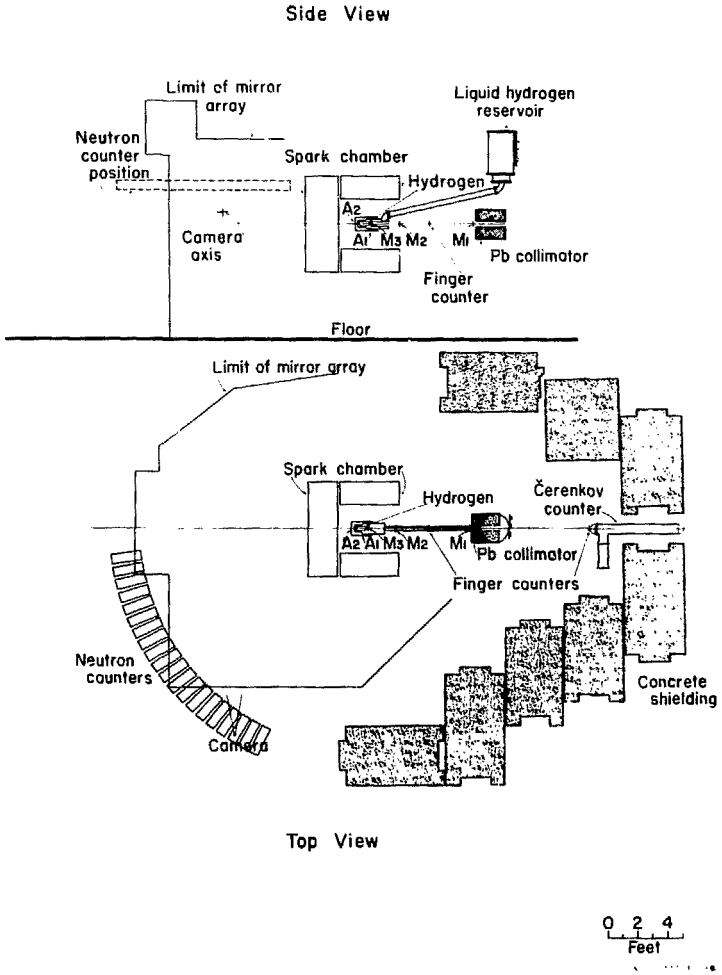

Fig. 1. The Experimental Apparatus

E. The Pion Beam

The beam transport system directed negative pions from an internal target in the Bevatron onto our liquid hydrogen target. A diagram is shown in Fig. 2. The physical placement of the beam magnets was severely restricted by the requirement that the beam start in the internal Bevatron beam and pass through the center of the cube determined by our spark chambers, preferably at right angles to the rear chamber. We used the same magnets and magnet positions as were used in the previous experiment[13]. The higher beam momentum required higher fields in all magnets and some experimentation with the target position inside the Bevatron, since the fixed Bevatron field could not be scaled with momentum.

The transport system was divided into halves. In the first half, the internal proton beam of the Bevatron hit a 0.25- by 0.50- by 8.0-in. aluminum target. Secondary particles emerging with an angle near 0° with respect to the angle of the incident protons were diverted by the Bevatron field and passed along the experimental beam line. They were collected by a quadrupole doublet (Q_1), which focussed them through the steering magnet (B_1) and onto a 1-in. high by 2-in. wide brass collimator at the center of the field lens (Q_2). Q_1 had a large (12-inch diameter) bore and was placed closest to the Bevatron in order to

maximize the flux through it, but this meant that in practice it was a steering magnet as well as a lens. This caused the first half of the beam to give inadequate momentum selection, and to be very hard to tune.

Particles emerging from the field lens went through a 40° bend (B_2) and were focussed by a triplet lens (Q_3), through a 4- by 4-in. lead collimator, 24 in. long, and onto the liquid hydrogen target. Final momentum selection was done by this part of the beam.

Field values of B_2 were determined by wire-orbiting, since B_2 determined the momentum. The effect of the Bevatron field was calculated by numerical integration, using the measured values of the field in a computer program BOFUS.[14] The results from BOFUS were used as the starting point for program OPTIK[15], which calculated the necessary field values for the other magnets. The OPTIK values were then adjusted experimentally for optimum results. The final values for the second half of the system were quite close to those predicted by OPTIK. The difference was probably due to the vertical focussing properties of the 40° bend, which OPTIK does not treat correctly. The Bevatron fringe field has not been measured well, so its effect was not calculated accurately, and the first half of the beam required a certain amount of trial-and-error. The final tuning method adopted was, first, to set the bending magnets to the desired values, which

were determined by the total bend, and turn all the quadrupole lenses off, to ensure that they would not also act as steering magnets and change the beam momentum. Second, the target inside the Bevatron was moved to maximize the flux delivered to the liquid hydrogen target under these conditions. When this maximum was achieved, the Bevatron field directed particles from the internal target out along the desired beam line. Third, the lenses were turned on and tuned to focus particles from the internal target onto the collimator, and from the collimator onto the liquid hydrogen target. Finally, the field lens was turned on to the values calculated by OPTIK, since the field lens had little effect and an error in its setting was small compared to the defocussing in the rest of the beam.

This system delivered negative pions in a spot 3 in. high and 5 in. wide at the entrance of the 4 by 4-in. collimator. Particles which hit the collimator would have to pass through 24 in. of lead before reaching the target or spark chambers. Further selection by the final scintillation counter M_3 resulted in a momentum acceptance of $\pm 1.0\%$. The divergence was $\pm 0.8^{\circ}$ horizontally and $\pm 0.4^{\circ}$ vertically. The number of pions depended directly on the number of protons which hit the internal target in the Bevatron, and was usually about 600,000 during a Bevatron pulse of 1.5 seconds. The beam rate was then 400 kHz.

At the end of data-taking, the electron and muon contamination of the beam was measured with a high-pressure methane Cerenkov counter, which has been described in detail elsewhere[16]. A diagram is shown in Fig. 3. The beam composition was different at different momenta. It is summarized in Table I.

Table I. Beam Composition

E(MeV)	P(MeV/c)	Electron	Muon	Pion
1604	880	27%	3%	70%
1632	930	22	5	73
1661	980	10	4	89
1688	1030	7	4	89
1716	1080	4	4	92
1743	1130	3	4	93

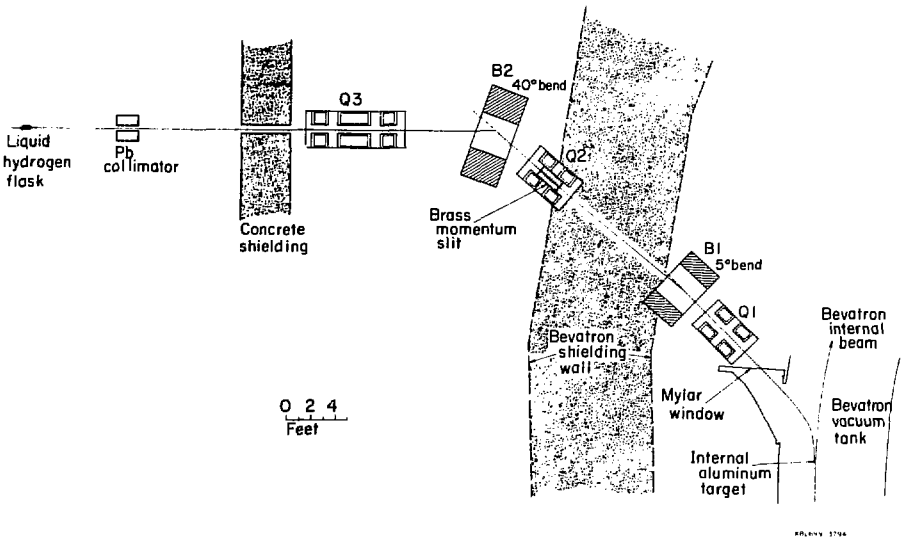

Fig. 2. The Pion Beam

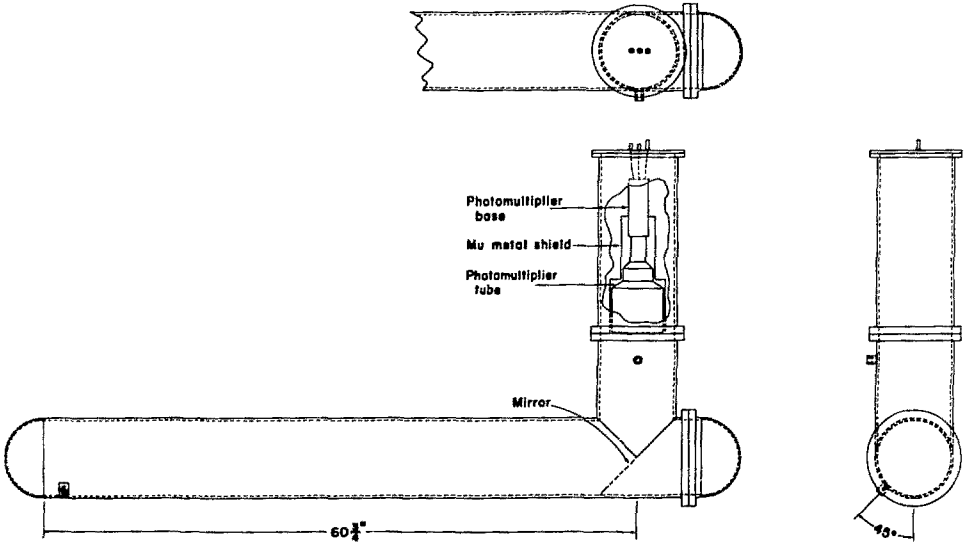

Fig. 3. Schematic of the Cerenkov Counter

C. The Liquid Hydrogen Target

The pion beam passed through a target of liquid hydrogen which was located approximately at the center of the spark chamber array. The construction of the target has been described in detail by Risser[17], and his figures are reproduced here. (See Fig. 4 and 5.) The flask itself was a Mylar cylinder, 8 in. long and 4 in. in diameter. In order to place the hydrogen supply plumbing upstream and out of the kinematically preferred regions, and at the same time to put the last beam counter close to the hydrogen target, the vacuum jacket was a cylinder extending 8 in. upstream beyond the flask, with a reentrant hole for the counter.

The entrance and exit windows of the liquid hydrogen flask and of the vacuum jacket were in the beam line. The flask was made of 7.5-mil Mylar, and the jacket windows of 10-mil Mylar. With the target empty, the flask material seen by the beam had a thickness of 0.123 g/cm^2. The electronics could also have been triggered by interactions in the last beam counter, which was a disk of scintillator 1/16-in. thick, making 0.167 g/cm^2, and from some depth into the veto counter (A_2), which was placed in the beam behind the flask. By contrast, the hydrogen in the flask had a thickness of 0.149 g/cm^2.

Typical interaction rates were 0.73% of all incoming particles with the flask full of liquid hydrogen, and 0.09% with the flask empty.

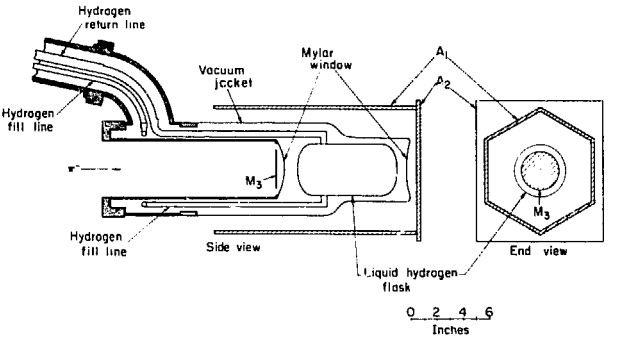

Fig. 4

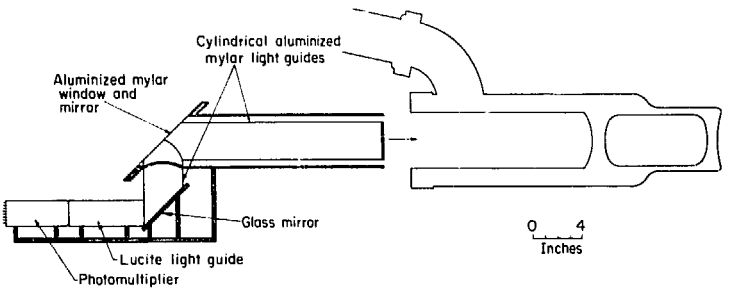

Fig. 5

XBL 6910-5779 A

Fig. 4 and 5. The Target and Surrounding Counters

D. The Scintillation Counters

All the scintillation counters were made from "Pilot B" scintillator, which is polyvinyltoluene doped with p-terphenyl and p,p' diphenylstilbene.

The beam-defining counters (M_1, M_2, M_3) and the veto counters surrounding the liquid hydrogen target (A_1, A_2) were viewed by RCA 6575 photomultiplier tubes. All had light guides of twisted Lucite strips between the scintillator and the phototube, except M_3, which was the last counter before the target. Because of the physical construction of the target, the light from the M_3 scintillator had to pass upstream in the beam line before being diverted out to the phototube. For this reason, the light guide for M_3 was a cylinder of aluminized Mylar filled with air, and a 45° mirror of 1/2-mil aluminized Mylar across the beam line reflected the light toward the phototube. The construction of M_3 and its position near the target are shown in Fig. 5.

Each beam-counter scintillator was a plane disk. The size decreased as the beam converged on the target, M_1, M_2, and M_3 being 4, 3.5, and 3 in. in diameter, respectively. The scintillator for M_1 was 1/2 in. thick, so it gave a relatively large number of photons at the passage of a beam particle. The timing of the pulse output of the M_1 phototube was therefore quite stable with respect to the passage of the particle, and it was used to determine the timing of

the beam in subsequent logic circuitry. The H_2 and H_3 scintillators were each 1/16-in. thick, to minimize scattering. The H_2 and H_3 signals were used only for coincidence logic, where the timing was not as critical.

The veto counter surrounding the hydrogen target (A_1) was a hexagonal cylinder made of 1/4-in. scintillator and viewed by three phototubes. The veto counter downstream of the target (A_2) was an 8-in. square of 1/4-in. scintillator. The veto counters are shown with the target in Fig. 4.

There were four separate rectangular gamma-ray detection counters, partially covering the open (upstream) face of the spark chamber cube. Each was a sandwich of eight sheets of 1/4-in. scintillator alternating with eight sheets of 1/8-in. lead. They were positioned so that a photon from the center of the liquid hydrogen target would hit a gamma counter if it were going in a direction to miss more than half the thickness of the spark chambers. The inner hole was made large enough to pass the beam and avoid extraneous interactions. Their sensitivity was set to detect a minimum-ionizing particle passing through any one of the eight scintillator sheets.

E. The Neutron Counters

The twenty neutron counters were also scintillation counters made from "Pilot B", but their operation was somewhat different from the other counters, and more complex, so a separate section is devoted to them. A diagram is shown in Fig. 6.

Each neutron counter was a cylinder of scintillator 8 in. long and 8 in. in diameter. They were viewed by Amperex XP1040 photomultiplier tubes, which are 5 in. in diameter. The light guides from scintillator to phototube were truncated lucite cones. The face toward the liquid hydrogen target was covered by a 10-in. square veto counter (V). Each veto counter was viewed through a twisted lucite light guide by either an RCA 8575 or an RCA 6810 photomultiplier tube, since limited numbers of each were available.

The design of the neutron counters and their associated electronics has been described in detail by Risser[18]. The experiment required not only detection of neutrons but also accurate timing information. A neutron is detected by looking for the light produced in the scintillator by a recoil proton. The energy deposited in the scintillator by the proton depends on the energy it receives from the neutron, and on the distance it can travel before leaving the scintillator. These factors were examined by the method of Kurz by a computer program called TOTEFF,[19] which uses measured

cross-sections for neutrons on carbon and hydrogen, plus the geometry of the scintillator and threshold information for the photomultiplier tube and its electronics to calculate the average detection efficiency of the neutron counter as a function of neutron energy. The results for the conditions of this experiment are shown in Fig. 7.

The energy threshold depended on the tube voltage. The correct voltage to produce the threshold used by TOTEFF was determined by looking at the pulse height spectrum given in detecting electrons produced in the scintillator by the 2.62 MeV gamma rays from a Th^{228} source. The tube efficiency tended to change with time. When it was properly set by looking at the pulse height spectrum from a Th^{228} source which could be placed next to the counter, the counter was exposed to another Th^{228} source which was pneumatically driven from inside a lead shield on the floor of the experimental area and about ten feet from the neutron counters. The counting rate was recorded. Thereafter, the threshold could be set by adjusting the tube voltage to reproduce this counting rate, without examining the pulse height spectrum. This adjustment was normally done once a day, which was adequate to eliminate significant fluctuations in the neutron counter efficiency.

Accurate timing information required that the timing be determined by some process which was

independent of the amplitude of the pulse given by the photomultiplier tube, since this amplitude varies widely due to statistical fluctuations in the number of photons detected and changes in the energy deposited in the scintillator by the particles detected. To provide a signal with better timing than a simple discriminator would give, the following scheme was used. The signal from the last dynode of the phototube triggered a high-threshold discriminator, which produced a 60-ns negative "pedestal" with a level just below the threshold of a second discriminator. Another signal was formed by delaying the signal from the anode and passively adding it to an attenuated signal from the dynode. The result was a bipolar pulse which started positive and then went negative with a steep slope. This was added to the "pedestal", and the sum was a signal which crossed the threshold of the timing discriminator with a steep slope, at a time which was almost independent of the eventual size of the original pulse.

The timing uncertainty using this method was ±1.0 ns.

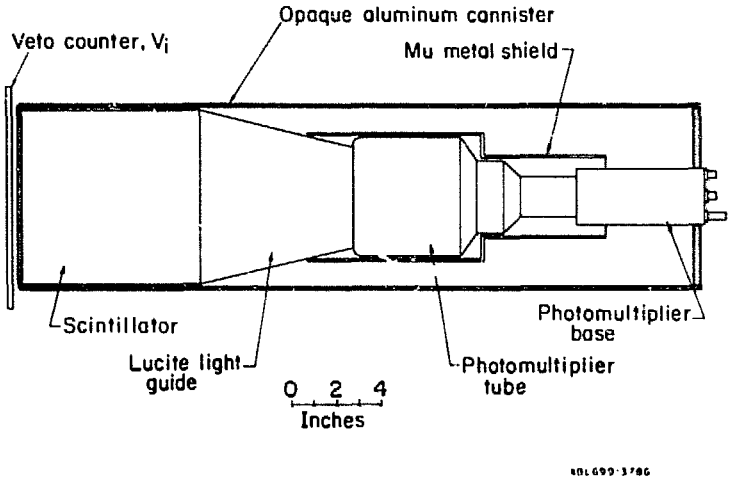

Fig. 6. A Neutron Counter

Figure 7. Neutron [illegible]

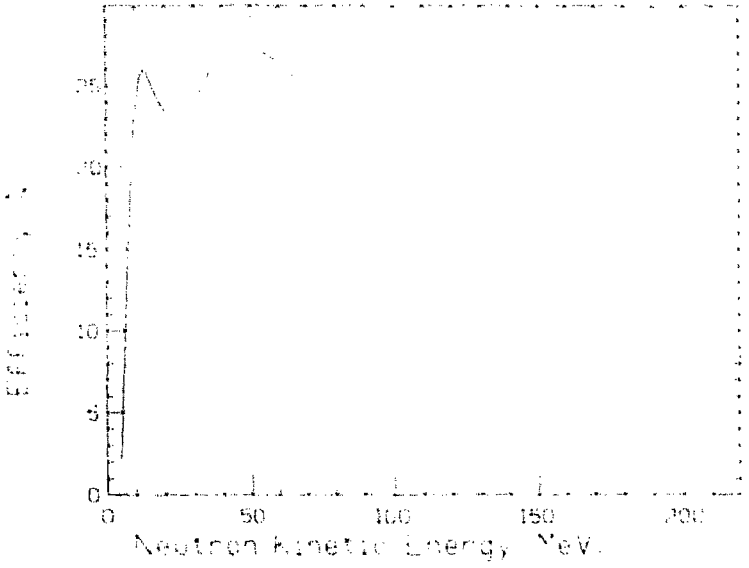

XBL 751-[illegible]

F. The Spark Chambers and Optics

The spark chamber system, with its associated electronics and mirror maze for optical viewing, was built for a previous experiment, and was not changed. A detailed description can be found in the published results of that experiment[20], and in published descriptions of the spark chamber pulsed high voltage supplies[21].

The five chambers formed a cube surrounding the liquid hydrogen target. As described previously, the front face of the cube was open to admit the beam and partially closed by the gamma detectors of lead and scintillator.

Each chamber was assembled in modular form. The first module in each chamber was constructed with five 48-mil aluminum plates, in which the probability of photon conversion was low. Tracks occuring in the first module were generally assumed to come from charged particles. The rest of each chamber consisted of modules with lead plates. Each lead plate was 32 mils thick and laminated between two plates of 16-mil aluminum for strength. Each lead-plate module was made of six lead plates, followed by one aluminum plate to lie against the lead plate of the next module. The modules were constructed with optically clear Lucite frames and spacers. The gap spacing was 5/16 in. Each lead module had 0.915 radiation lengths of lead and a

total thickness of 2.3 in. The thinness of each lead plate increased the detection efficiency for low-energy photons.

The side chambers measured 48 by 60 in., and contained seven lead modules plus the aluminum module. The back (downstream) chamber was 78 by 78 in. and contained eight lead modules plus the aluminum module. The downstream chamber was electrically two different chambers, one 36 and the other 42 inches wide. A Lucite bar, one inch wide, separated the two parts. The position of the bar was staggered from module to module so that adjacent modules did not have adjacent dead areas.

Two orthogonal views of each chamber were photographed on a single frame of 35-mm film by a Flight Research camera. The data box and the Nixie lights to display the frame number were also photographed on the same frame. Fig. 8 shows the arrangement of the five spark chambers in space and on the film.

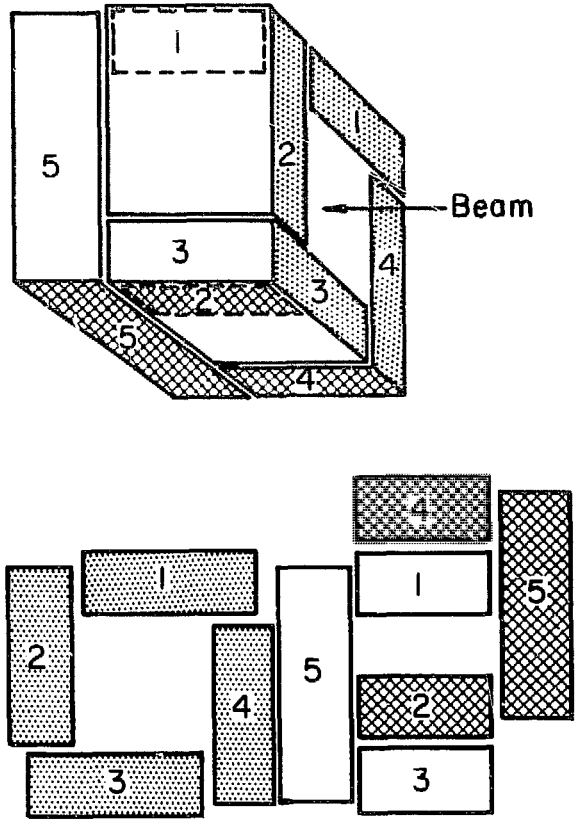

XBL699-3788

Fig. 8. The arrangement of spark chambers in space (top) and the arrangement of spark chamber views on film (bottom).

G. The Electronics and Trigger Logic

The electronic logic was designed to detect the following condition: an incoming beam particle, with no other beam particle near it in time, interacts with a target proton to produce a final state with no charged particles (a "neutral final state"). One of the particles, not travelling at the speed of light, is detected by a neutron counter. If this happens, the following events take place. High voltage is applied to fire the spark chambers. Switches are set to enable lights on the data box, encoding information about the identity of each counter which detected a particle, and the time of flight of the particle detected by the neutron counter. Fiducial lamps are lighted on the spark chambers. The data box is triggered, and all the previously enabled lamps are lit. The camera records the chambers and the data box. Finally, an 80 ms dead time is started, during which the film is advanced in the camera and the spark chamber high voltage capacitor banks are recharged. Half-way through the dead time, the data box light switches and the time-of-flight logic are reset. When the dead time ends, the whole system is ready to detect another event.

The logic is diagrammed in Fig. 9. An incoming pion produces a triple coincidence $B_1 B_2 B_3$ at the BEAM coincidence unit (B). It may also trigger any of the beam hodoscope counters, which are not required in the

logic, but are recorded on the data tox. Timing is arranged so that M_1, the most stable signal, is the last to arrive at BEAM, and determines the BEAM timing.

The M_1 signal also generates a dead-time signal (DT), which can veto the BEAM signal at the next coincidence unit, MONITOR (M). DT has two parts, generated by DT^1 and DT^2. DT^1 arrives at MONITOR 52 ns earlier than the beam signal, and has a duration of 50 ns. DT^2 arrives 2 ns later than the start of BEAM, and lasts for some 600 ns. Each BEAM signal then arrives at MONITOR along with a DT signal which vetos all other BEAM signals arriving close in time, but not within a window of 4 ns. One particle alone will be unaffected, but if two arrive close in time, but more than about 2 ns apart, each vetos the signal of the other, and neither is registered as a MONITOR. This arrangement prevented the jamming of electronics at the normally high beam rates, and reduced the probability that a track from one particle would be present in the spark chambers along with the photon tracks from another. It also helped to prevent accidental triggers, in which a veto counter detected one beam particle, but had not recovered sensitivity rapidly enough to detect a second.

An output signal came from MONITOR for each single beam particle detected. This signal went to the coincidence unit GC, where the target vetc counters were in anticoincidence. A GC output pulse signaled a

"neutral final state"--a reaction in which a beam particle, suitably separated in time from all others, entered the target region and no charged particles emerged.

Some data were taken for which only a neutral final state signal was required. Usually, however, there was a further requirement of a signal from one (or more) of the 20 neutron counters, which have been described in section E. The outputs from all twenty were fanned together at the unit SN, and the neutron coincidence unit (NC) detected coincidences between SN and GO. It accepted SN pulses with a wide distribution of times. The "prompt peak" contained a large number of events with the timing of particles travelling at the speed of light from the interaction in the target to the neutron counter. The GC pulse arriving at NC was 120 ns wide, timed to accept pulses from -30 to +90 ns, relative to the prompt peak. In order to reduce the picture-taking rate, a short pulse called the prompt-peak killer (PPK) was also generated from a GC and SN coincidence, but with timing determined by GO. The PPK signal was used to veto at NC all events in the prompt peak.

As will be seen in Table IV, some data were taken without the PPK veto ("PPK OUT"), as a possible check to be used in future analysis. Removing the veto increased the picture-taking rate by a factor of four or five, but it added only pictures with the wrong

neutron-counter timing. The net result was a decrease in useful data and scanning efficiency.

The decision to accept an event and fire the spark chambers was logically equivalent to an output pulse from NC. In order to determine the neutron counter timing, two more logic units were used. NC output was standardized by a discriminator N, and clipped to obtain a pulse of definite duration, well-fixed in time with respect to the original neutron counter pulse. And a signal called FIRE required a coincidence of M_1, M_2, M_3, and N, with A in anti-coincidence. FIRE timing was determined by M_1. One output from FIRE and one from N were fed to a time-to-amplitude converter (TAC). The amplitude of the TAC output was measured by an analog-digital converter (ADC)[22], which used a successive binary approximation method to measure and digitize the input pulse height. The ADC output was a channel number from 0 to 4095, which was displayed in 12 lights on the data box. The ADC has essentially equal channel widths from channel 40 to 4000. It accepts input pulses less than 1 μs. long and produces its output in less than 25 μs. This combination of TAC and ADC gave a resolution of six counts = 1 ns, although uncertainties in the rest of the neutron counter system were larger.

FIRE output was also the signal to trigger the chambers, the data box lamps, the chamber fiducials, the camera, and the dead time, as described above.

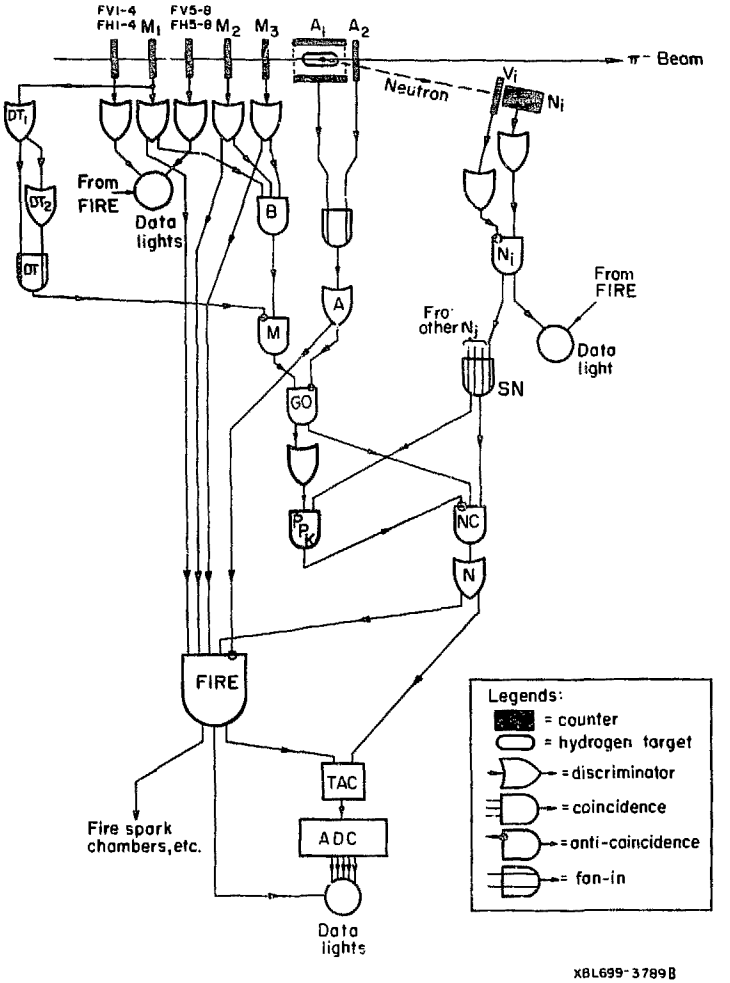

Fig. 9. The Electronics

F. The Data Box

The data box was an array of 96 Xenon flash lamps which were enabled by logic signals from any desired source, and triggered by the FIRE signal. It was designed to be scanned by the automatic scanning system, which also scanned the film for spark images. Lamps were set to display the frame number, the neutron time-of-flight, and the identity of each beam hodoscope counter, neutron counter, and gamma counter which was triggered. Other data could be set by an array of manual switches, but this was not found to be useful. As a check, one light was controlled by the data box logic, and was set to require that an even number of lights be lit.

III. Data Reduction and Analysis

A. Data Collection

Data collection for the experiment took place at the Bevatron of the Lawrence Radiation Laboratory in Berkeley, from February 19, 1969, to March 24, 1969. Set-up and tuning time was approximately three months. Much of the development and setup had been done for previous experiments.

Six different beam momenta were used: 880, 930, 980, 1030, 1080, and 1130 MeV/c, with approximately equal numbers of incident beam particles at each. In each case, the trigger requirement was a neutral final state plus a count in one (or more) of the neutron counters (the "NORMAL" trigger). In addition, the same amount of film as for each momentum was taken in a seventh condition (the "NFS" trigger), with a beam momentum of 1030 MeV/c and requiring a neutral final state but not the neutron counter.

Table II. Pictures Taken.

Total Energy (MeV)	Beam Momentum (MeV/c)	Trigger	Incident Particles	Neutral Final States	Pictures Taken
1604	880	NBM	2.008×10^9	11.43×10^6	37120
1632	930	NBM	1.952	12.57	42786
1661	980	NBM	1.982	16.93	60559
1688	1030	NBM	1.939	16.70	63858
1716	1080	NBM	2.237	16.49	65776
1743	1130	NBM	1.997	11.25	46891
1688	1030	NFS	2.776×10^6	23919	23919

B. Scanning

The film was scanned by the LBL Group A Scanning and Measuring staff. The scanners searched in the two views of each chamber to find matching arrays which could be interpreted as the two views of a shower. They recorded the total number of photons detected as showers or as counts in the gamma counters. They also recorded the location in each view of the position of the first spark of each shower, measured on a coarse grid corresponding to a spatial resolution of about 2 in. by 3 in.

There are many uncertainties in the scanning process. The shape of a shower in the chambers depends on the kinematic details of the pair-production, bremsstrahlung, and scattering processes which produce and absorb charged particles. In the ideal case, a shower appears in the chamber as a cone of sparks, with the vertex at the conversion point of the original photon, and expanding laterally as it goes deeper into the chamber. However, there are several effects which can alter this shape to the point where the sparks, if there are any, can't be identified as resulting from a photon. Especially in the case of photons with energy less than about 50 MeV, the electrons and positrons from the pair-production and bremsstrahlung may stop in the chamber material before they pass through many plates and gaps. The result is a shower with less than

three sparks, which can't be counted because of the confusion with spurious sparking in the chambers. In the case of photons with higher energy, the bremsstrahlung photons may go several inches before reconverting. The result appears to be a separate low-energy shower. In any case, spurious sparks can be produced by processes not associated with a photon, and be counted as showers. When there is more than one shower in one chamber, one may overlap another in one or both views, and the scanner must sort them out by matching each spark in one view with its mate in the other. This is a time-consuming and frustrating process, and one which invites error.

Besides the problems caused by the difficult decisions that the scanners had to make, there was the possibility of an outright blunder. A scanner could miss a shower completely, or make a mistake in recording the grid coordinates or even the chamber number. In order to estimate statistically the effect of scanner error, a sample of about 9000 frames was scanned three times by three different scanners. Their results were compared frame-by-frame, and in case of disagreement the frame was scanned by a physicist, who decided the "truth" for the frame. Truth in this case was determined by well-defined scanning instructions, in which each shower was examined separately and without reference to the other showers or to the apparent geometry of the event. (Almost all of the

detected reactions produced an even number of photons, but scanning with this information in mind would have produced biases. The scanner could include a marginal shower if it made an even number, or reject it if not, and if the final total was an odd number, he would perhaps take another look. For this reason, the scanning criteria could not involve the event geometry.)

This conflict-scan process gave a sample of 27,000 scans, together with a result for each scan that should have been reached by the scanner. In the case of two-shower events, which is the only sample used in the analysis for this thesis, the probability was 93.9% that the scanner would correctly identify the event. In addition, there was a certain probability that a scanner would mis-label as a two-shower event an event which in truth had some different number of showers. This added to the recorded number of two-shower events a number equal to 9.0% of the true number. The extra events could be rejected with high efficiency by kinematic analysis, but the unidentified two-shower events were lost, and a correction factor was used to account for them.

C. Measuring

The scan results, including the approximate locations of the showers, were keypunched onto IBM cards. These were fed to the Spark Chamber Analysis Library Program (SCALP)[23], which recorded them in packed format in a "masterlist" on magnetic tape. The film was scanned by the IBL SASS machine[24], a precision cathode-ray tube and photomultiplier system driven by a Honeywell DDP-24 computer, controlled by program FLICKERS.[25]

FLICKERS first scanned the area of the film in which the data box appears, and decoded the spots it found as lights on the data box. It then scanned the area where the chambers appear, and recorded the positions of all spots it found, supposing that these were the images of the chamber sparks. FLICKERS was designed to ask for operator intervention if it finds something obviously wrong, like a parity error on the data box or missing fiducial lights, but it does not do sophisticated error checking.

The FLICKERS output tape, with its information about the location of sparks, was fed to the CDC 6600 computer system, running program DHARMA-HANDSCAN[26]. DHARMA-HANDSCAN read the SCALP masterlist for an event to find the approximate location of each shower, as recorded by the scanner. It then processed the FLICKERS tape information for the same event, looking

for sparks corresponding to showers in the given positions. If DHARMA-HANDSCAN found sparks that it could call a shower, it recorded on an output tape the position of the first spark and the direction of that shower.

The ultimate goal was to have a program (DHARMA) which would analyze FLICKERS output information and reconstruct the shower positions and directions without guidance from the scanners. However, this has proved to be a very difficult problem, due to the great variations in the appearance of showers in the chambers, to the presence of spurious sparks which must not be identified as showers, to air spaces which separate shower segments in real space, and to the problems of matching two views, in which overlapping of different showers may occur. DHARMA was not used in obtaining the results presented in this thesis.

D. Kinematic Analysis

The measurement information from DHARMA-HANDSCAN was fed to SPSUE[27], an adaptation for spark-chamber physics of SIOUX[28], a kinematic analysis program. SIOUX does kinematic fits of the measured particle energies and directions to predetermined hypotheses as to the number and identities of the interacting particles. It requires energy-momentum conservation and assumes that the measured quantities have gaussian errors.

The result of a fit is the energy-momentum vector, with errors and correlations, for each particle in the hypothesis, plus χ^2 values that indicate how much the data had to be changed in order to reach a physical solution.

The most difficult problem in interpreting the results of these fits is in deciding the biases that are introduced, and trying to eliminate or correct them. For this thesis, fits were done to the hypothesis

$$\pi^- p \rightarrow n \gamma\gamma$$

For the final distributions, all of the experimental information was used, and the gamma-gamma mass was constrained to be that of the eta. For evaluation of background and resolution, one or more quantities, such as the gamma-gamma mass or the neutron time-of-flight, were left unconstrained. The difference between the

value of a quantity, calculated from a measurement, and the value calculated by SICUX without using that particular measurement, gave a good indication of the reliability of the fit.

E. The Monte-Carlo Calculation

1. General Considerations

A Monte-Carlo program was written for the L.B.L. computers, to analyze the effects of geometry and kinematics on the detection efficiency for various reactions. The program generates large numbers of events of any topology with any desired production and decay distribution for each particle, and examines the behavior of the resulting neutron and photons. Cuts and weighting factors can be applied to simulate the effects of experimental apparatus, and the result is an output tape similar to the tape produced by DHARMA, but with the "truth" for each event as well as the measured quantities. There is also provision for histogramming in the program, to avoid the complication and delay of tape handling. In the early stages of the analysis, the Monte-Carlo output was used for evaluating the performance of SPSUE, and adjusting some of the SPSUE parameters. Its use for this thesis is to provide an estimate of the overall detection efficiency as a function of production cosine, which is used as a factor to correct the observed distribution of detected events and give the distribution of events actually produced in the target. The rest of this section is a description of some of the parts of the Monte-Carlo calculation.

2. Event Generation

Events were generated by my adaptation of SAGE II[29], a subroutine package for generation of Monte-Carlo events with any number of produced particles, and distributions corresponding to phase-space or a part of it, to a Breit-Wigner formula, to a "peripheral phase-space" distribution, or to a combination of them. The events could be further weighted to give any desired cross-section, although this is inefficient if the additional weights differ greatly from a constant.

For each event, the package produced the momentum four-vectors of each particle, in the laboratory and center-of-mass systems. The final neutron and photon laboratory vectors were then used in subsequent calculations.

3. Neutron-Lead Scattering

The scattering of the neutron in the material of the spark chambers, through which it had to pass before reaching the neutron counters, was estimated using total cross-sections of Lindenbaum[30]. The angular distribution for non-elastic scatters was assumed isotropic for angles less than 30°, zero beyond. Results were not sensitive to this shape, since the reduced neutron velocity and increased path from hydrogen target to neutron counter caused SIOUX to reject the event in any case. The angular distribution for elastic scatter was calculated using the diffraction peak in a black disk approximation[31]. The total effect was evaluated as part of the Monte-Carlo calculation. In each generated event, the neutron path was generated from the hydrogen target, through the chambers, and to the final hit or miss of a neutron counter. Multiple scattering was allowed, simply by repeating the scattering calculation starting at each new scattering point, until the neutron either stopped or escaped the chambers.

4. Neutron Counter Efficiency

The probability that a neutron counter would detect a neutron which hit it was calculated as described in Section II E, and expressed as a function of neutron kinetic energy, shown in Fig. 6. It is approximately 21% at high energies, but rises higher at energies below 100 MeV. It falls again at energies below 18 MeV, but these energies are kinematically impossible in the eta-production reaction, at our experimental beam momenta.

5. Spark Chamber Efficiency

For each photon entering the material of the spark chambers, the cross-section for conversion on aluminum and lead was found, and used to generate a distance traversed in material before the shower started in the chamber. A "mathematical shower" was generated, with properties based on the behavior of experimentally observed showers caused by photons of the same energy. The mathematical shower consisted of regions where charged particles were present, and would make sparks in a chamber, and regions where they were not. This was then compared to the spark chamber construction, starting at the conversion point and continuing along the direction of the shower. In the regions of active chamber, sparks were "seen". In the other regions, where the shower had no charged particles or the chamber had a dead area, no sparks were allowed. The final result was a good estimate not only of the visibility of the shower, but of the number of sparks. It allowed an estimate of the effect of cuts on the number of sparks in the experimental events.

6. Sioux Efficiency

If measured values differ in a gaussian way from the true values, and if the resolution of the experimental apparatus is understood, and if the positions and properties of the experimental equipment are carefully measured, then the fraction of events rejected by any cut in X^2 or confidence level is calculable and, hopefully, small. The confidence level distribution is ideally flat, and usually rises below the 1% level, due to poorly measured events.

However, in this experiment, many quantities had measurement errors which were obviously not gaussian. For instance, the neutron direction is known to point toward the neutron counter, but any position on the counter is equally likely. (In SPSUE, the approximation was made that the measured direction was the counter center, and the uncertainty was an R.M.S. approximation to the counter radius.) The photon energy was measured by counting the number of sparks seen, and multiplying by an obliquity factor and an average energy-per-spark, but the uncertainty in this measurement is somewhere near a factor of 2.0. (To bend this measurement into something that could be approximated as gaussianly distributed, the logarithm of the energy was taken as the basic measured quantity.) To evaluate the effect on real data of the fits by SPSUE, data generated by the Monte-Carlo program were analyzed also. The resulting SPSUE

"detection efficiency" was treated as one more correction factor to be applied to the data.

F. Background Subtraction

In general, the multiple constraints imposed by SPSUE were sufficient to eliminate totally any background events. However, one class of spurious events can pass even the strict SPSUE criteria. It is possible that following a good eta production event, in which a slow neutron is produced and both the neutron and the eta go forward in the laboratory reference frame, the neutron counter is triggered well before the neutron should arrive, by charged particles produced by one of the photons. This effect becomes visible if a SPSUE fit is done, without using the measured time-of-flight information. In this case, the fit to an event gives a prediction of what the time-of-flight should be, and comparing with the measured times shows a relatively large number of events of the above class, with long predicted times and short measured times. It is very difficult to measure, because of the small number of events, but there must also exist a smaller background of good events with a spurious neutron counter trigger which comes near the correct time, in an event which would not otherwise cause a neutron counter trigger. Obviously, these events cannot be rejected by SPSUE on kinematic grounds. The only method of estimating this background is to make a plot of the measured time-of-flight against the time-of-flight predicted from all the rest of the kinematic

information, and to extrapolate this distribution from the region of unequal times to get an estimate of the background in the region where the (spurious) measured time-of-flight is equal to the time-of-flight required by the event kinematics. The uncertainty on this estimate is large, but fortunately the subtraction is small. The only region which is affected corresponds to a large range in neutron time-of-flight, but to a production cosine only from 0.9 to 1.0.

G. Differential Cross-Section

The analysis was done in two parallel operations, as described above. The kinematic analysis of the real data, done primarily with the program SPSUE, produced a number of events, for which all the measured information fit the eta-production hypothesis, and which are binned according to the production cosine calculated from the fit. This distribution of production cosines, containing between 300 and 900 events at each momentum, was modified only by a small background subtraction.

In an independent computer job, a large number of Monte-Carlo events with a flat angular distribution was generated and used to determine the bin-by-bin probability that an event produced in the target would be detected as a two-shower event, and that the resulting measured event would be identified by SPSUE as fitting the same event hypothesis. (A second question, of course, is whether SPSUE would give the correct production cosine. Analysis by SPSUE of Monte-Carlo events, for which the "truth" was known, showed that the resolution in production cosine was better than half the width of the bins used, so this resolution was not used in later calculations.)

For sorting the events into bins in production cosine, the width of the bins was decided somewhat indirectly. The Monte-Carlo studies showed that for

production angles in the backward hemisphere, which sent fast neutrons toward one of the small-angle counters, each neutron counter covered a different range of production cosine, with little or no overlap. In this range, a natural binning scheme of one bin for each neutron counter was used, despite the difference in bin width. On the other hand, events with scattering angles in the forward hemisphere tended mainly to send neutrons at large angles in the lab system. Each counter in the lab covered a relatively large range in the c.m. system, and the counter that was hit depended on the location of the interaction along the 8-in. length of the target as well as on the c.m. production angle. In the forward hemisphere, therefore, ten equal bins were taken in production cosine.

The total number of eta events in each bin, produced but not necessarily detected by the experimental apparatus, was found by comparing the Monte-Carlo events with the real data, using the proportionality

$$\frac{\text{DATA (detected)}}{\text{DATA (total)}} = \frac{\text{MC (detected)}}{\text{MC (total)}}$$

where, for each bin,
DATA (detected) is the number of real events seen,
DATA (total) is the total number of real events,
MC (detected) is Monte-Carlo events seen,
and MC (total) is total Monte-Carlo events.

Since the events were generated isotropically, MC(total) is simply the fractional size of the bin times the total number of Monte-Carlo events generated in the entire range from -1 to 1.

$$MC(total) = MC \times (DC/2.)$$

where MC is the total number of Monte-Carlo events,
and DC is the range of cosines covered by the bin. (DC is not well defined, since the range covered by each neutron counter depends on several kinematic factors. It cancels out in the next calculation, so this is not a problem.)

The differential cross-section is given by

$$\frac{d\sigma}{d\Omega} = \frac{DATA(total)}{I} \frac{A}{\rho N d} \frac{1}{2\pi DC}$$

where DATA(total) = number of events produced in the cosine range DC,
I = total effective incident pion flux,
d = length of the liquid hydrogen target (20 cm),
A = atomic weight of hydrogen (1.01 g/g-atom),
ρ = density of liquid hydrogen (0.0708 g/cm^3),
and N = Avogadro's number (0.6024 x 10^{24} atoms/g-atom).

Finally, the differential cross-section in each bin is

$$\frac{d\sigma}{d\Omega} = \frac{DATA(detected)}{MC(detected)} \cdot \frac{MC}{4\pi} \cdot \frac{A}{\rho N d}$$

The numbers used in determining the total effective incident pion flux are given in Table III. Various correction factors were necessary because of experimental and analytic effects not contained in the above formula. They are described in the following section and in Table IV. The final values for differential cross-section are given in Table V.

B. Corrections

1. Corrections to Incident Flux

Unanalyzed Pictures

Some of the pictures taken were lost or unusable, and some of the two-shower events which were found in scanning were not analyzed, due to computer problems. Both these effects mean that the number of incident pions which produced the events which were analyzed was smaller than the total number which were counted by the experimental electronics. The factors for each separate energy and trigger condition are found in Tables III.

Beam Contamination

The incident beam particles were not all pions. Muons and electrons could also pass down the beam channel and were counted, but would not react to produce a trigger. The beam composition was shown in Table I. The pion flux is the measured beam flux times this factor.

Extraneous Interactions of the Beam in the Target

As the pion beam passed through the liquid hydrogen target, some of the pions interacted to produce final states other than the ones of interest. The cross-section for all such pion-proton interactions is about 50 mb. A pion that interacted was no longer available to produce an eta, so the effective pion flux was smaller than the measured flux. The fraction scattered over the whole length of the target is $(S/I) = (\sigma \rho N d/A)$, where S is the number of scattered pions, σ is the $\pi^- p$ total cross-section, and the other symbols are defined above. This is 7.0%. The average fraction scattered before reaching any point was half of this, or 0.035, and the total effective flux must include a factor of (1. - 0.035) = 0.965.

Table IIIa. Effective Flux Calculation for 880 MeV/c

Target "PPK"	Full IN	Empty IN	Full OUT	
Beam Particles (MONITOR)	2.008	0.500	0.206	x 10^9
Neutral Final States (GO)	11.43	0.4048	1.166	x 10^6
Pictures Taken	37120	1279	14561	
Pictures Scanned	37106	1279	8568	
Two-Shower Events Seen	15392	461	4124	
Two-Shower Events Analyzed	14610	438	3653	
Corrections to Incident Flux				
for pictures not scanned	.9996	1.0	.5698	
for two-shower events not analyzed	.949	.950	.8858	
for beam contamination	0.70	0.70	0.70	
for extraneous beam interactions	0.965	0.965	0.965	
Total Effective Beam Flux	1.287	0.321	0.073	x 10^9
(Treating PPK In and Out together)	1.360	0.321		x 10^9
Eta Events Found by SPSUB	856	11		

Table IIIb. Effective Flux Calculation for 930 MeV/c

Target "PPK"	Full IN	Empty IN	Full OUT	
Beam Particles (MONITOR)	1.952	0.500	0.144	x 10^9
Neutral Final States (GG)	12.57	0.4138	0.929	x 10^6
Pictures Taken	42786	1349	12421	
Pictures Scanned	40960	907	0	
Two-Shower Events Seen	18046	419	0	
Two-Shower Events Analyzed	17538	419	0	
Corrections to Incident Flux				
for pictures not scanned	.957	.672		
for two-shower events not analyzed	.972	1.0		
for beam contamination	0.73	0.73		
for extraneous beam interactions	0.965	0.965		
Total Effective Beam Flux	1.279	0.237		x 10^9
Eta Events Found by SPSUE	602	5		

Table IIIc. Effective Flux Calculation for 980 MeV/c

Target "PPK"	Full IN	Empty IN	Full OUT	
Beam Particles (MONITOR)	1.982	0.621	0.145	x 10^9
Neutral Final States (GO)	16.93	0.6015	1.248	x 10^6
Pictures Taken	60559	2231	18135	
Pictures Scanned	58087	1468	2925	
Two-Shower Events Seen	25892	727	1519	
Two-Shower Events Analyzed	24068	694	1492	
Corrections to Incident Flux				
for pictures not scanned	.959	.658	.161	
for two-shower events not analyzed	.930	.955	.982	
for beam contamination	0.89	0.89	0.89	
for extraneous beam interactions	0.965	0.965	0.965	
Total Effective Beam Flux	1.518	0.335	0.020	x 10^9
(Treating PPK In and Out together)	1.538	0.335		x 10^9
Eta Events Found by SPSUE	514	7		

Table IIId. Effective Flux Calculation for 1030 MeV/c

Target "PER"	Full IN	Empty IN	Full OUT	
Beam Particles (HCBITOR)	1.939	0.500	0.183	x 10^9
Neutral Final States (GO)	16.70	0.4744	1.578	x 10^6
Pictures Taken	63858	1839	24382	
Pictures Scanned	49290	1292	0	
Two-Shower Events Seen	21731	521	0	
Two-Shower Events Analyzed	20462	451	0	
Corrections to Incident Flux				
for pictures not scanned	.772	.703		
for two-shower events not analyzed	.942	.866		
for beam contamination	0.89	0.89		
for extraneous beam interactions	0.965	0.965		
Total Effective Beam Flux	1.211	0.233		x 10^9
Eta Events Found by SPSUB	311	3		

Table IIIe. Effective Flux Calculation for 1080 MeV/c

Target "PER"	Full IN	Empty IN	Full OUT	
Beam Particles (RCNITOR)	2.237	0.668	0.148	x 10^9
Neutral Final States (GO)	16.49	0.6387	1.080	x 10^6
Pictures Taken	65776	2626	17229	
Pictures Scanned	44712	1847	0	
Two-Shower Events Seen	19934	722	0	
Two-Shower Events Analyzed	19487	707	0	
Corrections to Incident Flux				
for pictures not scanned	.680	.703		
for two-shower events not analyzed	.978	.979		
for beam contamination	0.92	0.92		
for extraneous beam interactions	0.965	0.965		
Total Effective Beam Flux	1.321	0.408		x 10^9
Eta Events Found by SPSUE	400	11		

Table IIIf. Effective Flux Calculation for 1130 MeV/c

Target "PPK"	Full IN	Empty IN	Full OUT	
Beam Particles (MONITOR)	1.997	0.519	0.213	x 10^9
Neutral Final States (GO)	11.25	0.4248	1.198	x 10^6
Pictures Taken	46891	1831	19596	
Pictures Scanned	44940	1493	3481	
Two-Shower Events Seen	16670	554	1645	
Two-Shower Events Analyzed	17354	495	1316	
Corrections to Incident Flux				
for pictures not scanned	.958	.815	.178	
for two-shower events not analyzed	.929	.893	.800	
for beam contamination	0.93	0.93	0.93	
for extraneous beam interactions	0.965	0.965	0.965	
Total Effective Beam Flux	1.595	0.339	0.027	x 10^9
(Treating PPK In and Out together)	1.622	0.339		x 10^9
Eta Events Found by SPSUE	431	6		

2. Target Empty Subtraction

Some of the events which passed all criteria for good eta events were in truth the result of interactions of the beam with the material of the target container, rather than with the liquid hydrogen. Data were taken with the liquid hydrogen drained from the flask to measure this effect. The rate of generation of good events with an empty flask is

Target Empty Rate (TE) = Good Events/Incident Flux

The Target-Full Rate is calculated similarly:

Target-Full Rate (TF) = Good Events/Incident Flux,

but this rate counts events generated in both the hydrogen and the flask. The rate of generation of events in hydrogen only (HO) is a simple subtraction:

HO = TF - TE.

The correction factor to go from a target-full measurement to a value for hydrogen only is

HO/TF = (TF-TE)/TF = 1. - TE/TF

The uncertainty in this factor is due mainly to the statistical uncertainty in the small number of passing events with target empty.

For instance, at 880 MeV/c, with target full 856 good events resulted from an effective incident flux of 1.360×10^9 incident pions. With target empty, eleven events resulted from 0.321×10^9 incident pions. The relative rate is

$$\frac{(11 \pm \sqrt{11}/0.321 \times 10^9)}{(856/1.360 \times 10^9)} = 0.054 \pm 0.016$$

The correction factor to be applied to the total cross-section is 1. minus this, or 0.946 ± 0.016.

The total number of target-empty events was so small--less than twelve for each energy--that no analysis could be done of the angular dependence. It is conceivable that rejection by SESUE, as a function of angle, of events generated in the flask was different than for events generated in the center of the target. This effect was not analyzed.

3. Miscellaneous Corrections to Cross-Section

Photon Conversion

Once an eta is produced and decays into two photons, each photon could possibly convert in the liquid hydrogen, aluminum, Mylar, or scintillator of the target and its veto counters. The signal from the electrons passing through the veto-counters mocked a charged final state, and no event was recognized. I estimate from the cross-section for photons on these materials, and from the target geometry, that each photon had a 3% chance of vetoing the event in this way. This means that the cross-section must be corrected by a factor of $(1./0.97)^2 = 1.063$.

Internal Conversion

Internal conversion, when one of the photons converts to an electron-positron pair in the original interaction, is usually considered part of the original $\eta \rightarrow \gamma\gamma$ decay, rather than a separate decay with a charged final state. According to Dalitz' formula[32], the probability for this is 1.62% (for either photon, not for each separately), so a correction of 1./0.9838 is needed in the cross-section.

Scanner Error

As discussed in Part B. of this Section, only 93.9% of the eta events were correctly identified by the scanners. A factor of 1./0.939 is needed in the cross-section. This excludes the possibility that a scanner labeled as a two-shower event one which was really something else, because SPSUE rejected these events with good reliability.

Shower Feed-Up

There was another possibility of losing an event. The two showers from an eta decay were sometimes accompanied by a third, left over from a previous event or a beam particle. With enough time, the clearing field applied to the chambers swept out all the ions left by previous events, but the sensitive time of the chambers was about 1 μs. The size of this effect was estimated by analyzing a sample of events with three showers, looking at each pair and trying to fit the event by a two-shower hypothesis. At the beam intensity at which our data were taken, the number of three-shower events which fit the two-shower hypothesis shows that 16% of the two-shower events are missing due to this "feed-up" effect. This requires another factor of 1./0.84 = 1.19 in the cross-section.

Partial Cross-Section

The final state detected for these calculations was a neutron and two photons, resulting from reaction (1), repeated here:

$$\pi^- p \rightarrow \eta n, \qquad (1)$$

and the decay (2):

$$\eta \rightarrow \gamma\gamma \qquad (2).$$

To find cross-sections for reaction (1), one must divide the results given in this paper by the ratio of the decay (2) to all eta decays[3]:

$$B(\eta \rightarrow \text{all decays})/B(\eta \rightarrow \gamma\gamma) = 2.63$$

Table IV. Corrections to Cross-Section

Target-Empty Subtraction

Momentum	880	930	980	1030	1080	1130 MeV/c
Target Full						
Events	856	602	514	311	400	431
Pions	1.360	1.279	1.538	1.211	1.321	1.622 x10⁹
Target Empty						
Events	11	5	7	3	11	6
Pions	0.321	0.237	0.335	0.233	0.408	0.339 x10⁹
Correction						
Factor	0.946	0.955	0.937	0.955	0.911	0.933
Error ±	0.016	0.020	0.024	0.026	0.027	0.027

Miscellaneous Corrections

for Photon Conversion	1.063
for Internal Conversion	1.016
for Scanner Error	1.065
for "Feed-Up" to Three Showers	1.190
for All Eta Decay Modes	2.63
Total Miscellaneous Corrections	3.602

Table Va. Differential Cross-Section for 880 MeV/c

Cosine Range	Fitted Eta Events	Backg'nd Events	Monte-Carlo Events	Differential Cross-Section (μb/sr)
-.95/-.90	91		76.5	216.6 ± 22.7
-.89/-.82	81		79.3	186.0 ± 20.7
-.70/-.60	88		75.9	211.1 ± 22.5
-.58/-.45	61		67.6	164.3 ± 21.0
-.43/-.29	60		66.0	160.7 ± 20.7
-.27/-.11	50		86.2	105.6 ± 14.9
-.10/0.	32		42.35	137.6 ± 24.3
.0 /+.10	22		40.25	99.5 ± 21.2
+.10/+.20	25		36.12	126.0 ± 25.2
+.20/+.30	31		37.93	148.8 ± 26.7
+.30/+.40	31		34.36	164.3 ± 29.5
+.40/+.50	30		31.86	171.5 ± 31.3
+.50/+.60	30		35.94	152.0 ± 27.8
+.60/+.70	25		43.12	122.5 ± 22.7
+.70/+.80	31		43.74	129.1 ± 23.2
+.80/+.90	44	2.8	35.41	211.9 ± 34.9
+.90/1.00	66	25.	47.28	127.1 ± 70.8

Result is based on a total effective beam flux of 1.360 x 10^9 pions, and includes a Target-Empty Subtraction factor of 0.946, and a factor for miscellaneous corrections of 3.602.

The error reflects only statistical uncertainties.

Table Vb. Differential Cross-Section for 930 MeV/c

Cosine Range	Fitted Eta Events	Backg'nd Events	Monte-Carlo Events	Differential Cross-Section (μb/sr)
-.95/-.91	72		63.7	212.9 ± 25.1
-.90/-.83	79		52.0	286.2 ± 32.2
-.72/-.63	50		58.1	162.1 ± 22.9
-.62/-.48	37		59.5	117.1 ± 19.3
-.47/-.34	35		62.9	104.8 ± 17.7
-.32/-.17	24		65.4	69.1 ± 14.1
-.15/+.01	33		70.7	87.9 ± 15.3
-.02/+.10	27		45.73	111.2 ± 21.4
+.10/+.20	19		34.50	103.7 ± 23.8
+.20/+.30	16		32.14	93.8 ± 23.4
+.30/+.40	17		26.40	121.3 ± 29.4
+.40/+.50	17		23.46	136.5 ± 33.1
+.50/+.60	16		26.71	112.8 ± 28.2
+.60/+.70	26		32.59	150.3 ± 29.5
+.70/+.80	18		33.47	101.3 ± 23.9
+.80/+.90	20	10.	28.92	110.7 ± 30.7
+.90/1.00	41	22.3	44.35	89.2 ± 50.4

Result is based on a total effective beam flux of 1.279×10^9 pions, and includes a Target-Empty Subtraction factor of 0.955, and a factor for miscellaneous corrections of 3.602.

The error reflects only statistical uncertainties.

Table Vc. Differential Cross-Section for 980 MeV/c

Cosine Range	Fitted Eta Events	Backg'nd Events	Monte-Carlo Events	Differential Cross-Section (μb/sr)
-.96/-.91	88		46.8	279.0 ± 29.7
-.90/-.84	52		58.3	132.3 ± 18.4
-.74/-.65	36		52.3	102.1 ± 17.0
-.63/-.52	26		58.4	66.1 ± 13.0
-.51/-.39	25		66.1	56.1 ± 11.2
-.37/-.24	26		58.1	66.4 ± 13.0
-.22/-.08	32		56.2	84.5 ± 14.9
-.07/+.09	28		46.8	88.8 ± 16.8
.0 /+.10	26		30.23	127.6 ± 25.0
+.10/+.20	21		27.89	111.7 ± 24.4
+.20/+.30	15		30.74	72.4 ± 18.7
+.30/+.40	16		27.66	85.8 ± 21.5
+.40/+.50	11		24.94	65.4 ± 19.7
+.50/+.60	12		27.59	64.5 ± 18.6
+.60/+.70	13		32.11	60.1 ± 16.7
+.70/+.80	13		30.41	63.4 ± 17.6
+.80/+.90	14	3.0	25.08	65.1 ± 23.8
+.90/1.00	32	18.	56.12	37.0 ± 28.1

Result is based on a total effective beam flux of 1.538×10^9 pions, and includes a Target-Empty Subtraction factor of 0.937, and a factor for miscellaneous corrections of 3.602.

The error reflects only statistical uncertainties.

Table Vd. Differential Cross-Section for 1030 MeV/c

Cosine Range	Fitted Eta Events	Backg'nd Events	Monte-Carlo Events	Differential Cross-Section (μb/sr)
-.96/-.92	35		51.8	139.7 ± 23.6
-.90/-.85	30		55.5	111.7 ± 20.4
-.75/-.66	13		60.6	44.3 ± 12.3
-.64/-.54	14		66.4	43.6 ± 11.6
-.53/-.41	10		52.0	39.7 ± 12.6
-.39/-.27	10		59.0	35.0 ± 11.1
-.25/-.11	17		58.1	60.5 ± 14.7
-.10/+.05	26		40.0	134.4 ± 26.3
.0 /+.10	14		25.13	115.2 ± 30.8
+.10/+.20	17		30.05	116.9 ± 28.4
+.20/+.30	14		30.33	95.4 ± 25.5
+.30/+.40	6		26.32	62.8 ± 22.2
+.40/+.50	13		22.79	117.9 ± 32.7
+.50/+.60	15		23.26	133.3 ± 34.4
+.60/+.70	15		27.63	112.2 ± 29.0
+.70/+.80	14		32.90	88.0 ± 23.5
+.80/+.90	15	3.0	37.17	66.7 ± 23.1
+.90/1.00	17	20.	46.73	0.0 ± 47.8

Result is based on a total effective beam flux of 1.211×10^{9} pions, and includes a Target-Empty Subtraction factor of 0.955, and a factor for miscellaneous corrections of 3.602.

The error reflects only statistical uncertainties.

Table Ve. Differential Cross-Section for 1080 MeV/c

Cosine Range	Fitted Eta Events	Backg'nd Events	Monte-Carlo Events	Differential Cross-Section (pb/sr)
-.96/-.92	15		59.5	45.9 ± 11.8
-.91/-.86	15		61.9	44.1 ± 11.4
-.76/-.67	11		76.9	26.0 ± 7.8
-.65/-.56	10		57.7	31.5 ± 10.0
-.54/-.43	16		52.9	61.9 ± 14.6
-.41/-.30	23		60.3	69.4 ± 14.5
-.28/-.15	22		68.25	58.7 ± 12.5
-.13/0.	33		52.05	115.5 ± 20.1
.0 /+.10	27		35.98	136.5 ± 26.3
+.10/+.20	20		31.16	116.7 ± 26.1
+.20/+.30	21		25.81	148.1 ± 32.3
+.30/+.40	31		25.12	224.6 ± 40.3
+.40/+.50	25		21.99	206.9 ± 41.4
+.50/+.60	31		28.94	194.9 ± 35.0
+.60/+.70	23		27.79	150.6 ± 31.4
+.70/+.80	26		24.84	190.5 ± 37.4
+.80/+.90	15	3.0	23.54	92.8 ± 32.1
+.90/1.00	29	21.	27.60	52.7 ± 77.8

Result is based on a total effective beam flux of 1.321×10^9 pions, and includes a Target-Empty Subtraction factor of 0.911, and a factor for miscellaneous corrections of 3.602.

The error reflects only statistical uncertainties.

Table Vf. Differential Cross-Section for 1130 MeV/c

Cosine Range	Fitted Eta Events	Backgrnd Events	Monte-Carlo Events	Differential Cross-Section (μb/sr)
-.96/-.92	16		45.6	51.3 ± 12.8
-.91/-.87	10		54.2	27.0 ± 8.5
-.77/-.68	6		76.9	15.9 ± 6.5
-.66/-.58	14		52.3	39.1 ± 10.5
-.56/-.45	26		63.7	59.7 ± 11.7
-.43/-.33	24		61.8	56.8 ± 11.6
-.31/-.19	33		52.85	91.4 ± 15.9
-.16/-.04	30		42.75	102.7 ± 18.8
.0 /+.10	30		27.23	161.1 ± 29.4
+.10/+.20	34		30.56	162.5 ± 27.9
+.20/+.30	27		25.49	154.9 ± 29.8
+.30/+.40	31		27.15	166.9 ± 30.0
+.40/+.50	35		31.83	160.8 ± 27.2
+.50/+.60	30		33.57	130.6 ± 23.9
+.60/+.70	24		32.37	108.4 ± 22.1
+.70/+.80	19		33.90	81.9 ± 18.8
+.80/+.90	20	3.5	40.83	59.1 ± 17.2
+.90/1.00	13	20.	35.59	0.0 ± 30.5

Result is based on a total effective beam flux of 1.622 x 10^9 pions, and includes a Target-Empty Subtraction factor of 0.933, and a factor for miscellaneous corrections of 3.602.

The error reflects only statistical uncertainties.

I. Fits to Sums of Legendre Polynomials

The measured values of the differential cross-section at each energy were fit, in the sense of minimum X^2, by a sum of Legendre polynomials, using a short program[33] running on the IBM 360/91 at SLAC. Fits through P_5 were done. Table VI shows the X^2 values resulting from the fit with each order polynomial, and the minimum acceptable order is indicated. The results are displayed in Table VII and Figs. 10. Full error matrices for the fit with fifth order are given in Table VIII.

The lowest necessary order is generally unambiguous. The lowest order giving a X^2/F less than 1.5 is the same as the order for which the confidence level first nears its asymptotic value, and coefficients of higher-order terms, in higher-order fits, are generally consistent with zero. In all cases, higher coefficients are within two standard deviations of zero, and these errors are computed only from the statistical uncertainties involved. In this sense, the question of which order to use is moot. In my tables and graphs, I have included the values and uncertainties for the high-order coefficients which are consistent with zero, in order to indicate an upper limit. It is my opinion that this is more useful than simply giving zero as the value, with no indication of the uncertainty.

Table VI. Goodness of the Fits

Chi-squared/Degrees of Freedom
(Confidence level)

Order		0	1	2	3	4	5
Beam Momentum (MeV/c)	C.M. Energy (MeV)						
880	1604	2.60 (.00)	2.19 (.00)	1.27** (.22)	1.37 (.17)	1.31 (.21)	1.20 (.28)
930	1632	4.08 (.00)	3.69 (.00)	1.77 (.04)	0.88** (.58)	0.89 (.56)	0.83 (.61)
980	1661	4.33 (.00)	3.88 (.00)	3.78 (.00)	2.08 (.01)	1.06** (.39)	1.02 (.42)
1030	1688	3.49 (.00)	3.43 (.00)	3.43 (.00)	1.10** (.36)	1.05 (.40)	1.07 (.38)
1080	1716	7.32 (.00)	2.44 (.00)	2.56 (.00)	0.95** (.50)	0.91 (.55)	0.89 (.56)
1130	1743	8.83 (.00)	5.49 (.00)	4.10 (.00)	0.67** (.81)	0.59 (.87)	0.62 (.83)

** Minimum Acceptable Order

Table VIIa. Results of the Fits

$$\frac{d\sigma}{d\Omega} = \sum_{\ell=0}^{\ell_{max}} A_\ell P_\ell(\cos\theta)$$ where P_ℓ is the Legendre polynomial.

Coefficient
(Error)

Coefficients are in μb/sr.

Beam Momentum (MeV/c)	C.M. Energy (MeV)	A_0	A_1	A_2	A_3	A_4	A_5
880	1604	152.4	-22.4	53.6			
		(5.9)	(11.0)	(13.8)			
		154.4	-22.4	50.6	4.1	-24.7	41.5
		(6.4)	(13.2)	(17.7)	(22.3)	(22.6)	(26.1)
930	1632	123.1	-42.6	63.9	-63.6		
		(5.9)	(11.6)	(14.3)	(17.4)		
		124.8	-41.8	62.4	-57.1	-14.2	30.5
		(6.1)	(12.0)	(15.7)	(19.8)	(20.7)	(24.1)
980	1661	86.9	-41.5	32.5	-62.1	57.2	
		(4.4)	(8.3)	(11.5)	(12.7)	(14.6)	
		86.5	-44.1	33.2	-67.6	58.4	-21.2
		(4.4)	(8.5)	(11.5)	(13.4)	(14.6)	(17.3)
1030	1688	77.3	5.5	-4.4	-86.9		
		(5.1)	(9.4)	(12.7)	(14.4)		
		77.8	2.8	0.5	-85.6	15.8	-17.0
		(5.3)	(9.9)	(13.5)	(17.3)	(19.1)	(19.4)
1080	1716	101.8	71.6	-39.4	-71.5		
		(6.0)	(11.5)	(14.8)	(14.3)		
		99.6	65.1	-53.1	-98.5	-37.1	-21.0
		(6.2)	(12.4)	(17.2)	(21.9)	(22.8)	(20.3)
1130	1743	87.3	37.1	-85.2	-79.4		
		(4.5)	(6.6)	(10.4)	(11.0)		
		88.1	35.6	-83.7	-72.0	13.7	-6.4
		(4.8)	(7.1)	(10.5)	(12.6)	(14.5)	(15.0)

Values are for $\pi^- p \rightarrow \eta n$, $\eta \rightarrow$ all decays.

Table VIIt. Results of the Fits

$$\frac{d\sigma}{d\Omega} = \lambda^2 \sum_{\ell=0}^{5} C_\ell P_\ell (\cos\theta)$$ where P_ℓ is the legendre polynomial.

Coefficient
(Error)
Coefficients are dimensionless.

Beam Momentum (MeV/c)	C.M. Energy (MeV)	C_0	C_1	C_2	C_3	C_4	C_5	
880	1604	1052	-153	344	28	-169	283	x10-4
		(44)	(90)	(120)	(152)	(154)	(178)	
930	1632	917	-307	458	-419	-104	224	x10-4
		(45)	(88)	(115)	(145)	(152)	(177)	
980	1661	681	-347	262	-533	460	-167	x10-4
		(35)	(67)	(91)	(106)	(115)	(137)	
1030	1688	653	24	4	-721	133	-143	x10-4
		(45)	(83)	(114)	(146)	(161)	(163)	
1080	1716	893	584	-477	-883	-332	-189	x10-4
		(56)	(111)	(154)	(197)	(204)	(182)	
1130	1743	838	338	-797	-685	131	-61	x10-4
		(45)	(67)	(100)	(119)	(138)	(143)	

Values are for $\pi^- p \rightarrow \eta n$, $\eta \rightarrow$ all decays.

Table VIII. Error Matrices for the Fits

These values correspond to the fits to fifth order in Table VIIa.

Units are $(\mu t/sr)^2$.

880 MeV/c

41.19	26.24	39.71	48.34	28.57	56.15
28.24	173.67	111.61	130.46	127.61	120.19
39.71	111.61	312.24	215.81	190.58	141.54
48.34	130.46	215.81	498.96	188.13	266.70
28.57	127.61	190.58	188.13	512.81	114.69
56.15	120.19	141.54	266.70	114.69	680.66

930 MeV/c

36.78	13.44	31.45	12.87	8.08	36.88
13.44	144.32	38.68	79.22	49.44	49.39
31.45	38.68	247.10	110.84	128.61	65.88
12.87	79.22	110.84	392.33	114.90	197.76
8.08	49.44	128.61	114.90	426.56	59.68
36.88	49.39	65.88	197.76	59.68	579.15

980 MeV/c

19.43	3.02	11.39	-3.01	16.20	6.83
3.02	72.86	-0.28	45.81	-0.60	36.37
11.39	-0.28	132.27	14.32	46.98	-9.55
-3.01	45.81	14.32	180.17	10.47	77.67
16.20	-0.60	46.98	10.47	213.82	-16.64
6.83	36.37	-9.55	77.67	-16.64	300.74

1030 MeV/c

28.32	21.37	10.36	-2.72	24.49	20.62
21.37	97.05	31.64	59.04	21.79	57.06
10.36	31.64	181.89	98.39	86.32	21.58
-2.72	59.04	98.39	299.91	162.96	144.00
24.49	21.79	86.32	162.96	364.22	153.95
20.62	57.06	21.58	144.00	153.95	375.42

1080 MeV/c

39.02	56.07	26.63	17.54	32.26	29.13
56.07	153.34	134.54	108.86	93.27	85.60
26.63	134.54	294.88	282.37	190.30	83.70
17.54	108.86	282.37	481.68	373.97	186.42
32.26	93.27	190.30	373.97	519.26	317.38
29.13	85.60	83.70	186.42	317.38	411.49

1130 MeV/c

22.85	17.25	-15.12	-7.64	21.01	17.94
17.25	50.16	16.62	3.14	14.26	39.54
-15.12	16.62	109.79	64.40	3.44	-14.09
-7.64	3.14	64.40	157.54	83.78	18.79
21.01	14.26	3.44	83.78	209.06	105.25
17.94	39.54	-14.09	18.79	105.25	224.81

Figure 10a 880 MeV/c

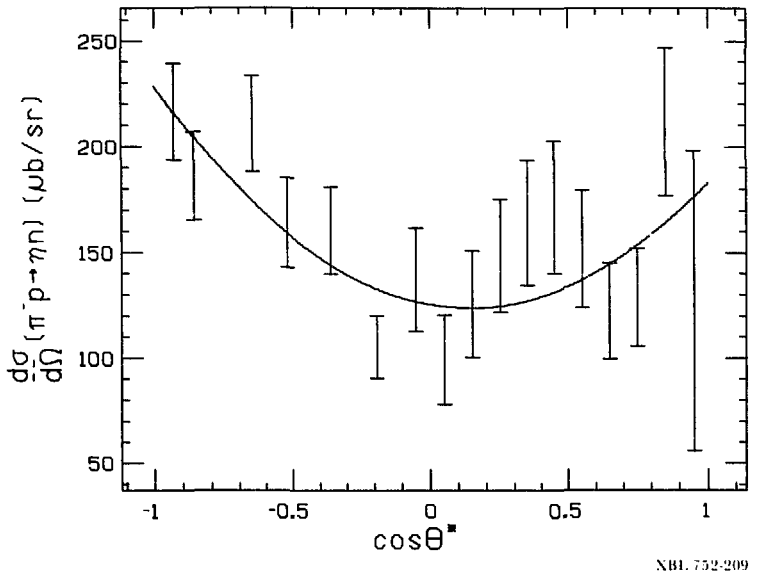

XBL 752-209

Figure 10b 930 MeV/c

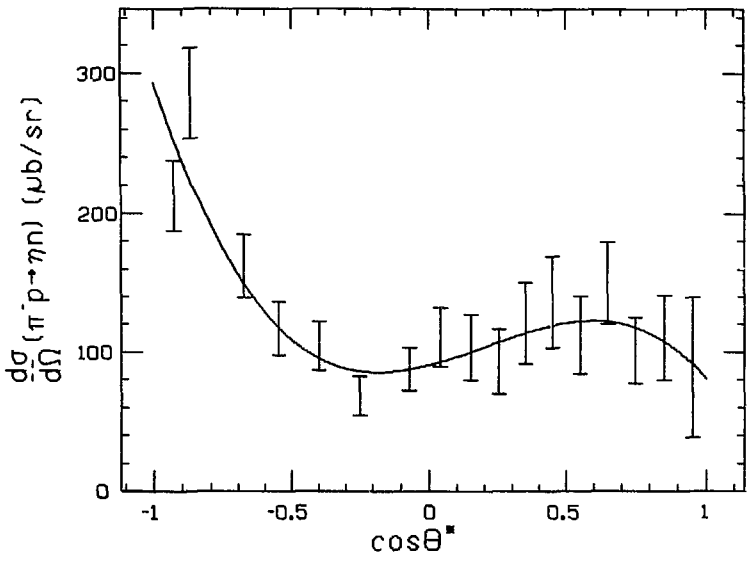

NBL 752-210

Figure 10c 980 MeV/c

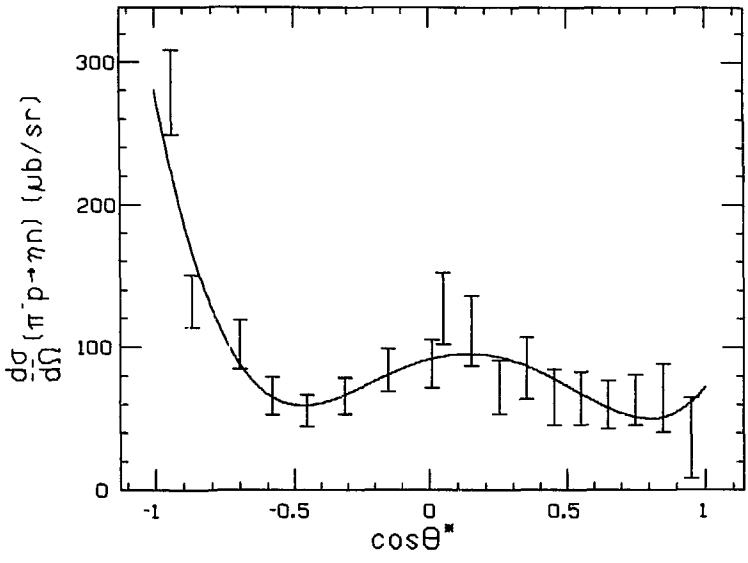

XBL 752-211

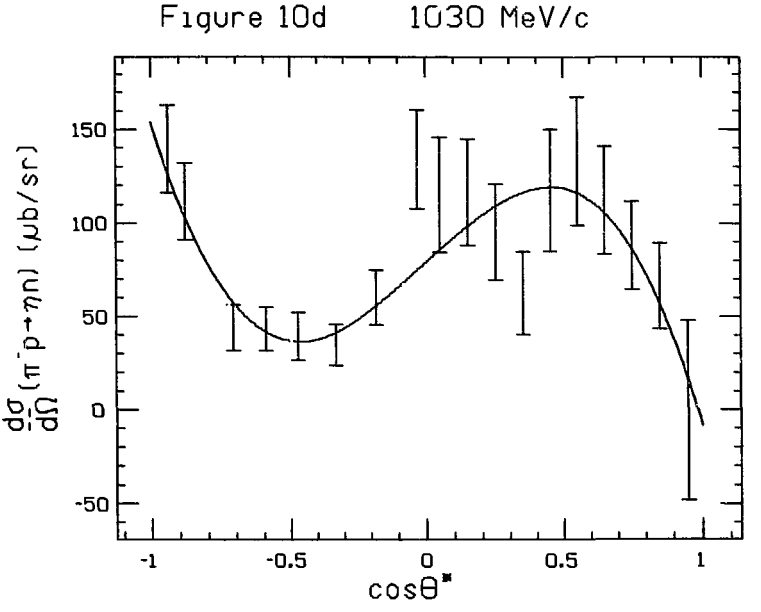
Figure 10d
1030 MeV/c
150
100
50
0
-50
-1
-0.5
0
0.5
1
cosθ*
dσ/dΩ (π⁻p→ηn) (μb/sr)

XBL 752-212

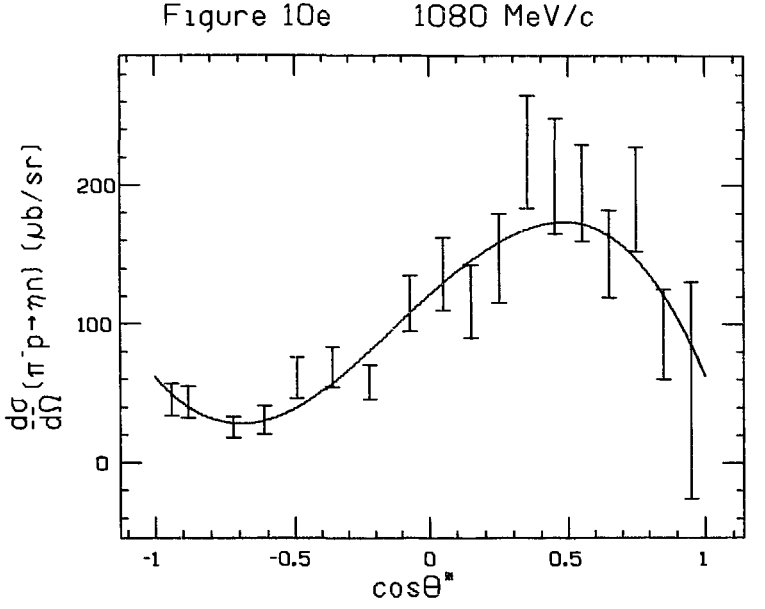
Figure 10e
1080 MeV/c
$\frac{d\sigma}{d\Omega}(\pi^- p \to \eta n)$ (μb/sr)
200
100
0
-1
-0.5
0
0.5
1
$\cos\theta^*$

XBL 752-213

Figure 10f 1130 MeV/c

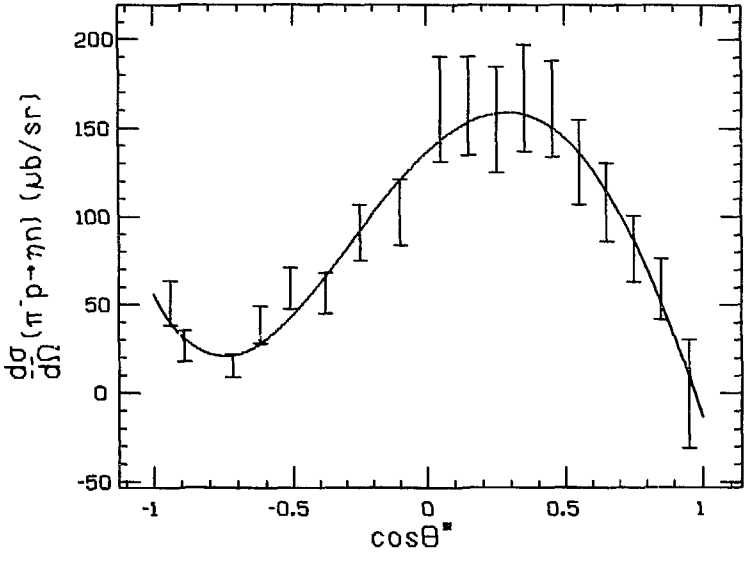

XBL 752-214

K. Total Cross-Section

Integrating the differential cross-section from the above fits gives

$$\sigma = \int_{\Omega} \frac{d\sigma}{d\Omega} d\Omega = 4\pi A_0 = 4\pi \lambda^2 C_0$$

Values are shown in Table IX.

No separate determination of the total cross-section, integrating over all angles, was done from the data reported here. The severe geometric bias of the neutron counters could be removed only by some process which considered the detailed geometry at each angle.

Separate data were taken at one momentum (1030 MeV/c), using the spark chambers but not the neutron counters. They have been analyzed by Nelson[34], with a method similar to that of Bulos et al.[3]. The result given is 419±33 μb, which is slightly higher than the result reported here.

Table IX also contains values for the differential cross-section at 0° and 180°, as extrapolated from the fits.

Table II. Calculated Cross-Sections

Beam Momentum (MeV/c)	C.M. Energy (MeV)	Total Cross-Section (μb)	Differential Cross-Section 0° (μb/sr)	180° (μb/sr)
880	1604	1915 (74)	183.5 (21.6)	228.4 (17.0)
930	1632	1546 (74)	80.8 (31.9)	293.2 (25.6)
980	1661	1092 (55)	73.1 (29.6)	280.4 (27.4)
1030	1688	971 (64)	-8.5 (27.5)	154.3 (19.5)
1080	1716	1280 (76)	62.6 (36.0)	62.4 (12.0)
1130	1743	1096 (57)	-40.2 (20.6)	44.3 (10.4)

Values are for $\pi^- p \rightarrow \eta n$, $\eta \rightarrow$ all decays.

Figure 11 Total Cross-Section

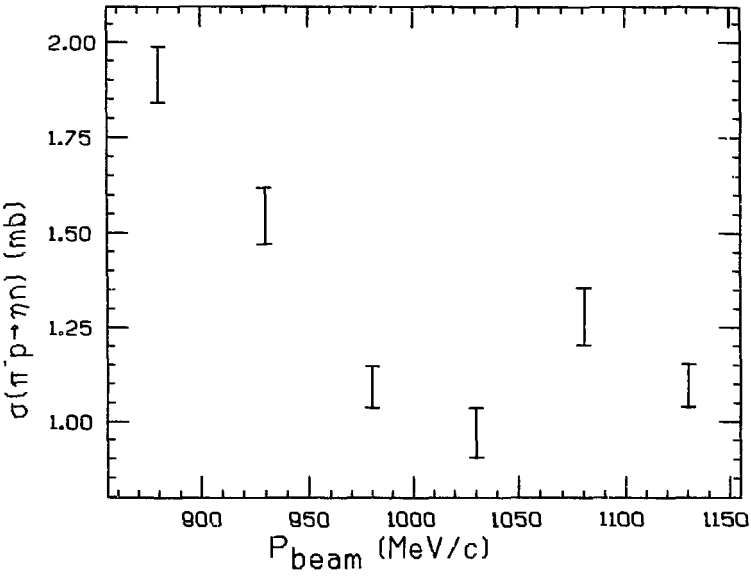

XBL 752-215

Figure 12a Cross-Section at 0°

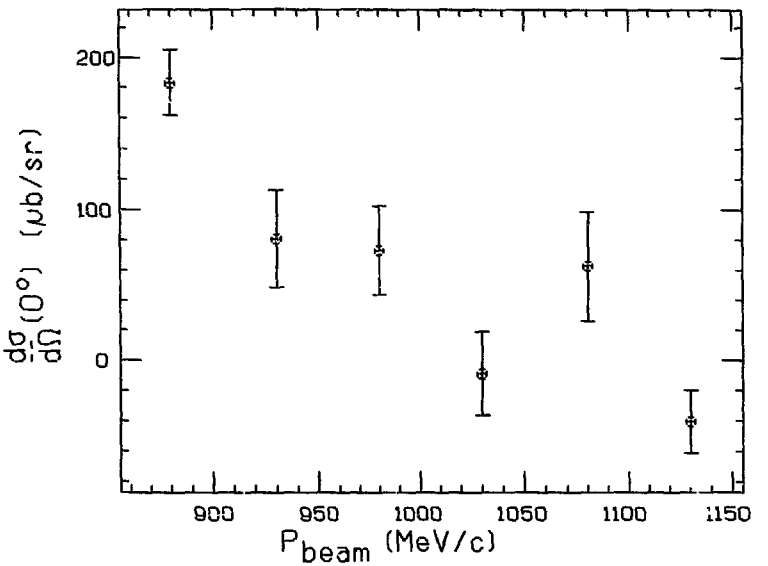

XBL 752-216

Figure 12b Cross-Section at 180°

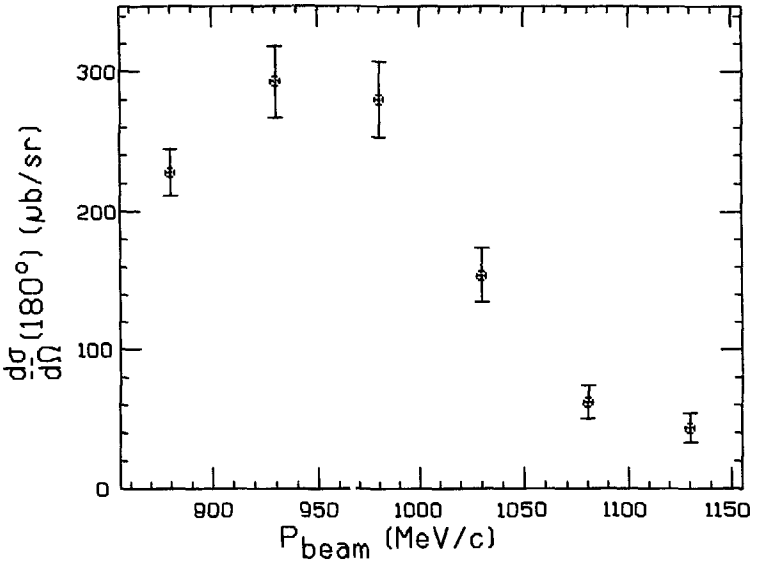

NBL 752-217

Figure 13a Legendre Coefficients

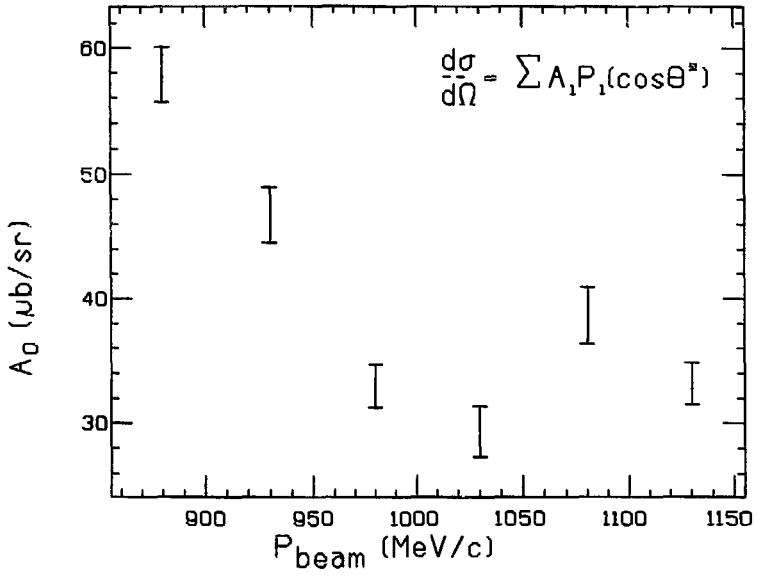

XBL 752-218

Figure 13b Legendre Coefficients

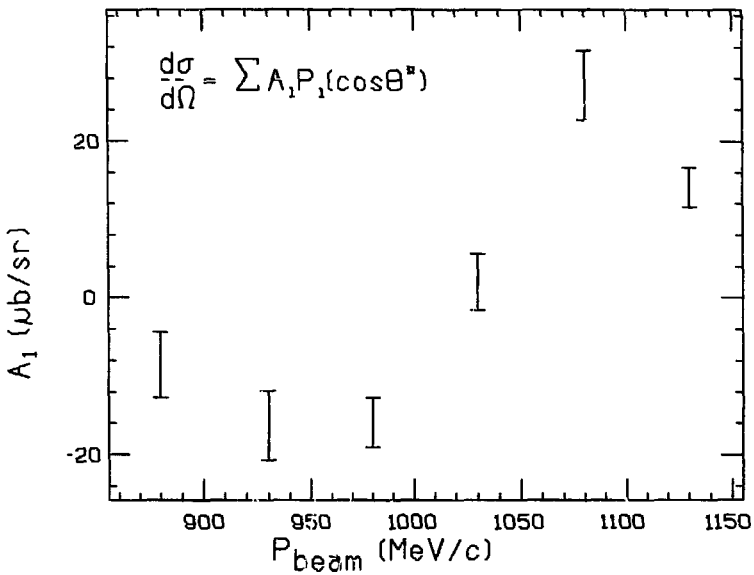

XBL 752-219

Figure 13c Legendre Coefficients

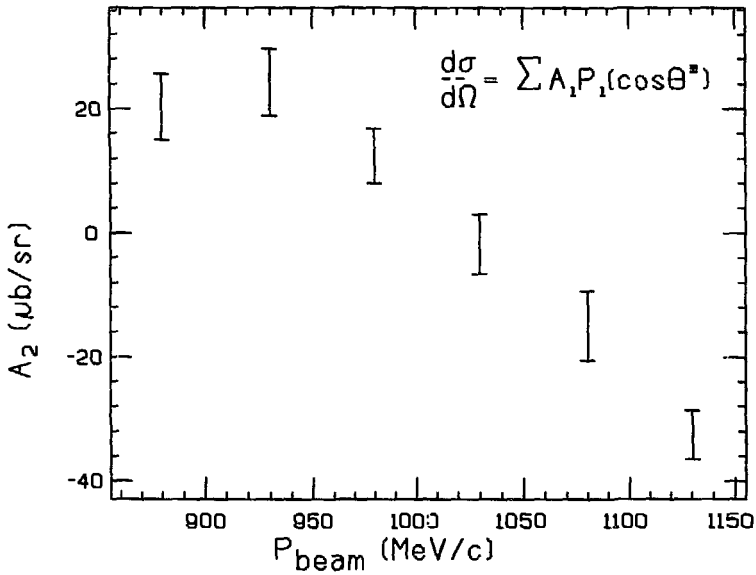

XBL 752-220

Figure 13d Legendre Coefficients

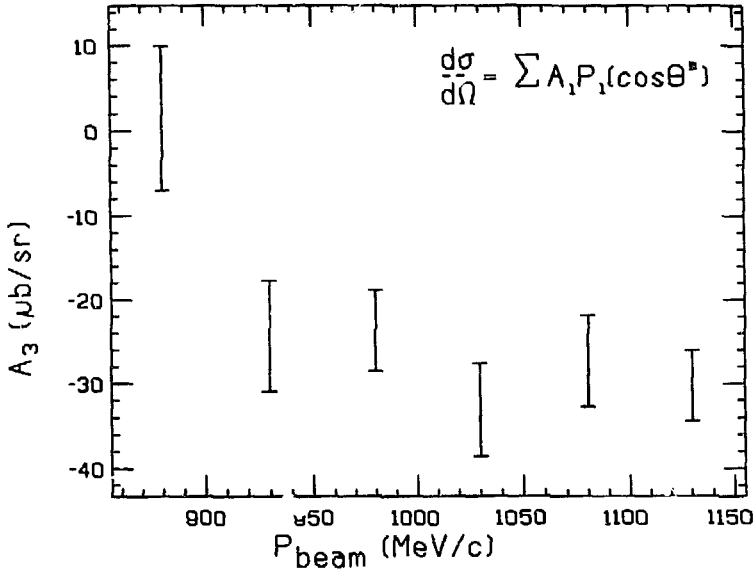

XBL 752-221

Figure 13e Legendre Coefficients

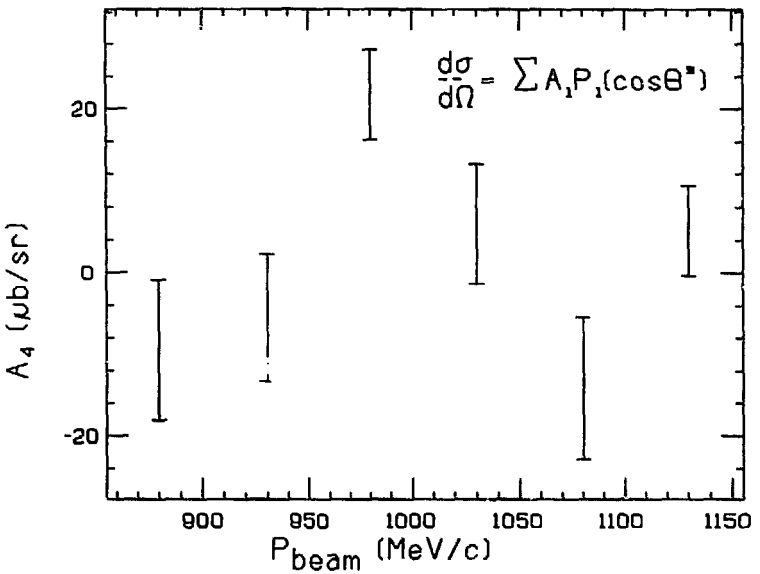

XBL 752-222

Figure 13f Legendre Coefficients

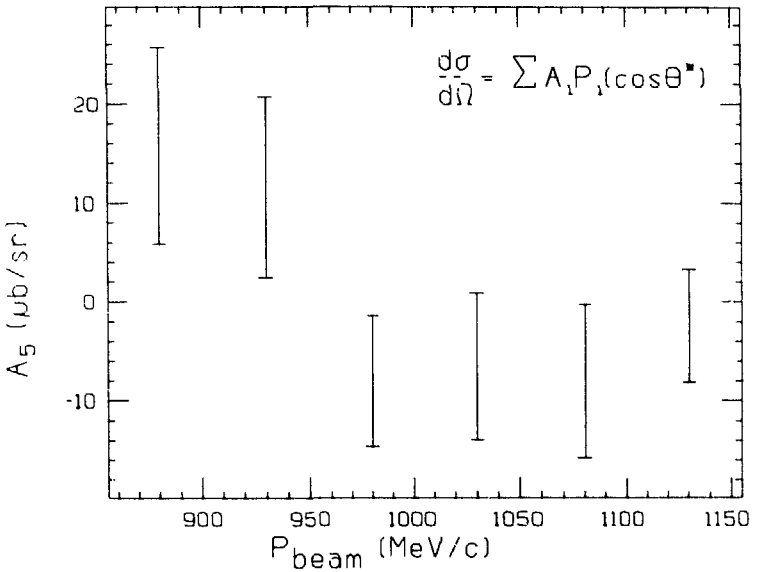

XBL 753-576

IV. DISCUSSION OF RESULTS

A. Comparison with Other Experiments

1. Total Cross-Section

Figure 14 shows the total cross-section for the reaction $\pi^- p \rightarrow \eta n$, as measured by this experiment and others[4-8]. Near threshhold, the cross-section rises linearly with the barycentric final-state momentum, indicating an s-wave interaction. A maximum of about 2.5 mb is reached. The cross-section falls again, to about 1.2 mb at 1000 MeV/c, then levels off. At the highest energy measured by Richards et al.[4], beyond the range of this experiment, it drops again, to about 0.66 mb, and then declines slowly out as far as 2400 MeV/c, according to Nelson's points. Uncertainties of this experiment are smaller than those of either Richards et al.[4] or Bulos et al.[5], and the points show more clearly what was indicated by the others, that there is a minimum at 980 and 1030 MeV/c, followed by a peak at 1080.

Figure 14a Total Cross-Section

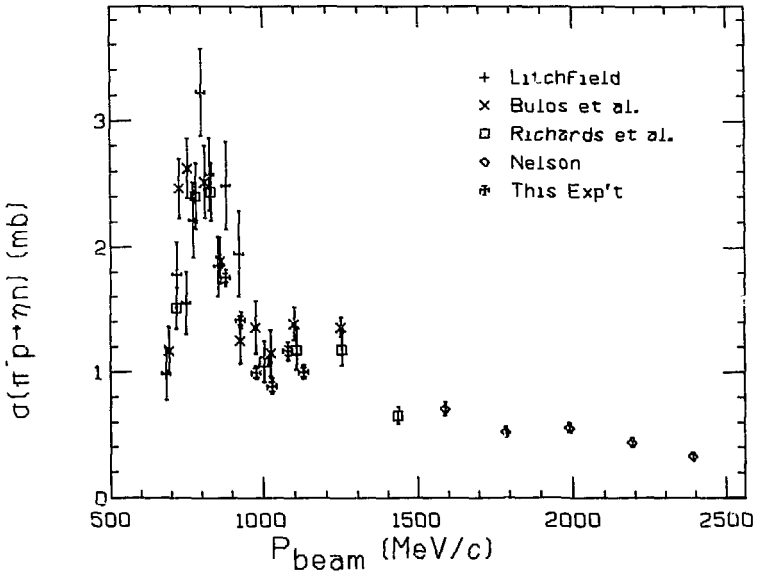

XBL 752-223

Figure 14b Total Cross-Section

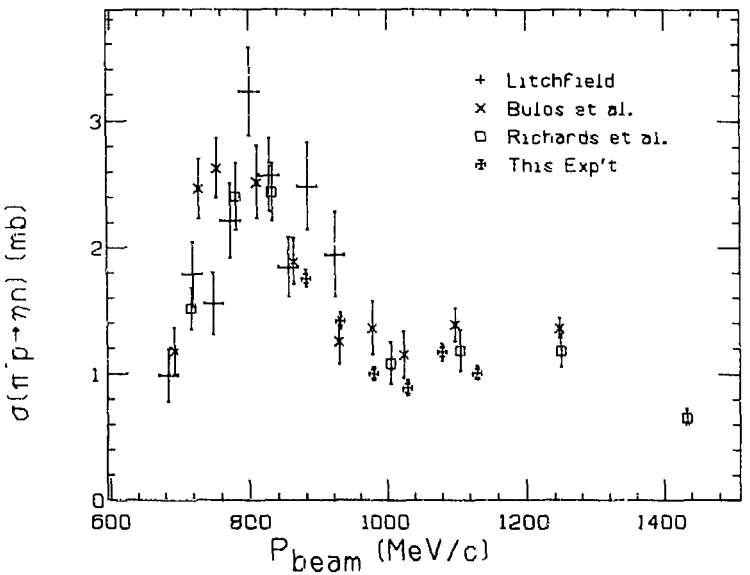

XBL 752-224

2. Differential Cross-Section at 0° and 180°

The values of the differential cross-section at 0° and 180° contain less information than parameters which describe the behavior of the interaction in the entire angular range. However, they are useful in comparing different experiments, and in comparing experiment with theoretical predictions. The differential cross-sections at 0° and 180°, found by extrapolation of the fits to Legendre polynomials, are shown in Figure 15, together with the results of others.

Figure 15a Cross-Section at 0°

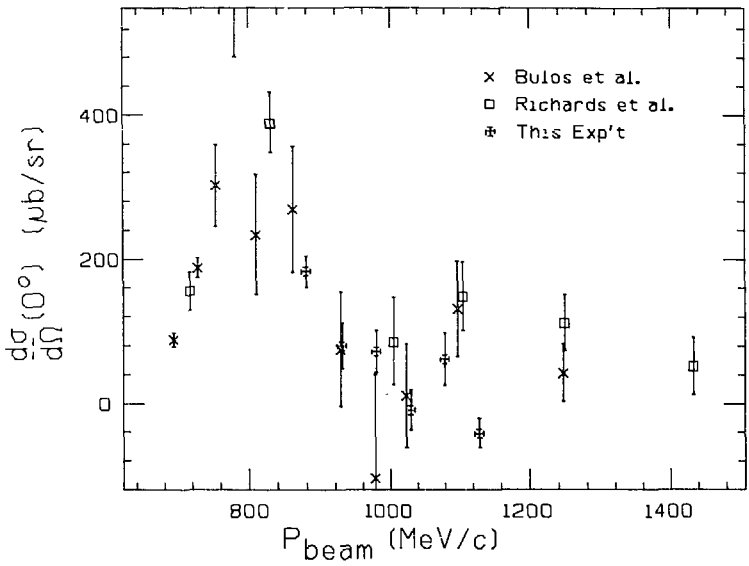

XBL 752-225

Figure 15b Cross-Section at 180°

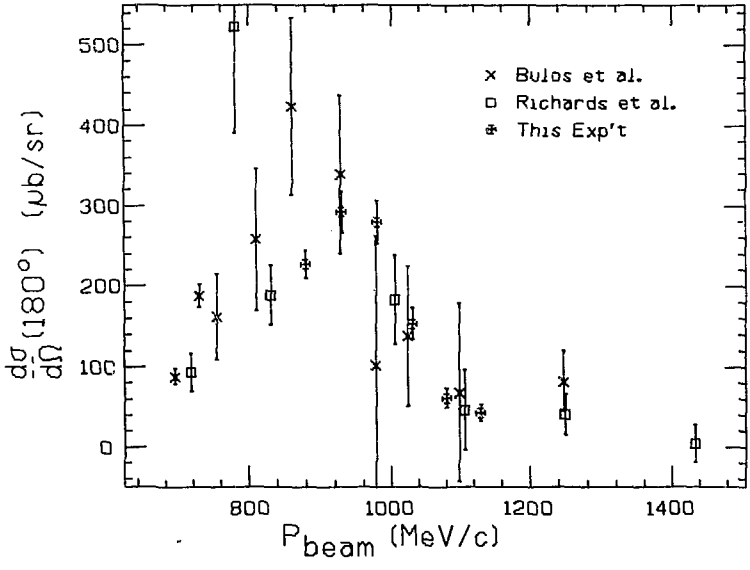

XBL 752-226

3. Legendre Polynomial Expansion Coefficients

Fig. 16 shows the coefficients C_ℓ in the expansion

$$\frac{d\sigma}{d\Omega} = \lambda^2 \sum_{\ell=0}^{5} C_\ell P_\ell(\cos\theta)$$

where λ is the reciprocal of the incident momentum in the barycentric system, and P_ℓ are Legendre polynomials. It shows values from other experiments. Richards et al. gave enough information in their paper for me to recalculate their fits, which I have done to get values for the coefficients beyond the orders they considered necessary. The solid curves in Fig. 16 are to aid the eye, and have no theoretical basis.

Except for a factor of $4\pi\lambda^2$, C_o is the same as the total cross-section. It is more easily seen here that the difference between 1000 MeV/c (1670 MeV total invariant mass) and 1200 MeV/c (1780 MeV) could be due either to a dip at the lower energy or a peak at the higher.

The values for C_1 emphasize a problem which was apparent in the total-cross-section and in C_o: the results of this experiment at the highest momentum, 1130 MeV/c, are not consistant with the results of other experiments. Nor are they the values one would expect from an extrapolation of the values at the other five momenta, although this is not sure because of the uncertainty of extrapolation. C_1 is slightly negative at 880 MeV/c, decreases to about -0.03 at 930 and 980 MeV/c, rises through zero at 1030 MeV/c to 0.06 at 1080

MeV/c, and may rise to 0.11 at 1150 and beyond.

The behavior of C_2 is more difficult to evaluate, because of larger uncertainties. It is zero below about 750 MeV/c (1530 MeV), rises to a maximum of 0.07 at 840 MeV/c (1580 MeV), then falls through zero at 1030 MeV/c (1690 MeV) to -0.04 at 1080 MeV/c (1715 MeV). The further behavior is uncertain.

C_3 is zero until slightly below the lowest energy of this experiment, then rises quickly to about -0.06, where it remains roughly constant from 930 MeV/c (1630 MeV) through the highest point of Richards et al.

C_4 is zero at 930 MeV/c and below, rises to a peak of 0.04 at 980 MeV/c (1660 MeV), and falls again to zero at 1080 MeV/c (1715 MeV). It seems to remain near zero, although Richards detects a value of -0.06 at his highest energy.

C_5 is zero, within the limits of experimental error.

Figure 16a Legendre Coefficients

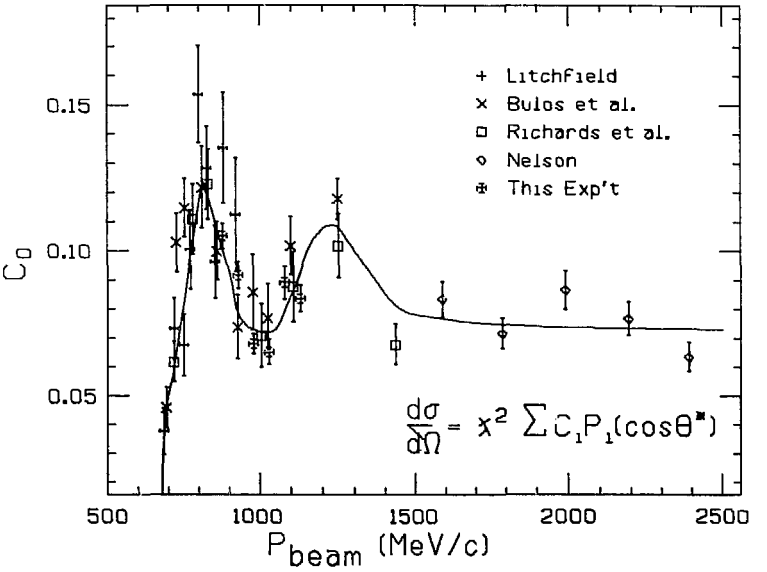

XBL 752 227

Figure 16b Legendre Coefficients

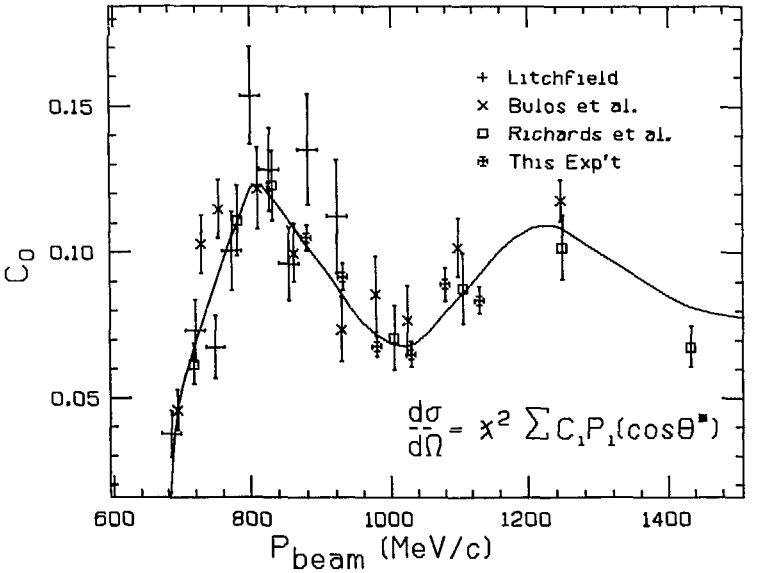

XBL 752-228

Figure 16c Legendre Coefficients

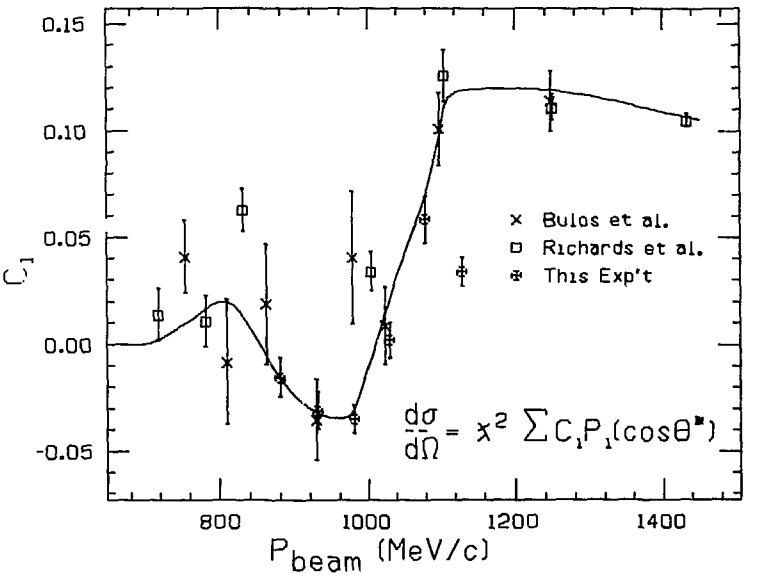

XBL 752-229

Figure 16d Legendre Coefficients

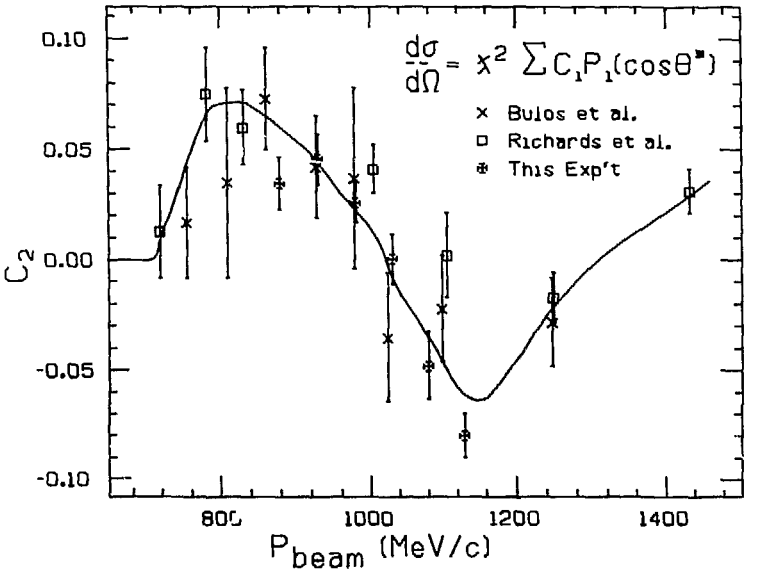

XBL 752-230

Figure 16e Legendre Coefficients

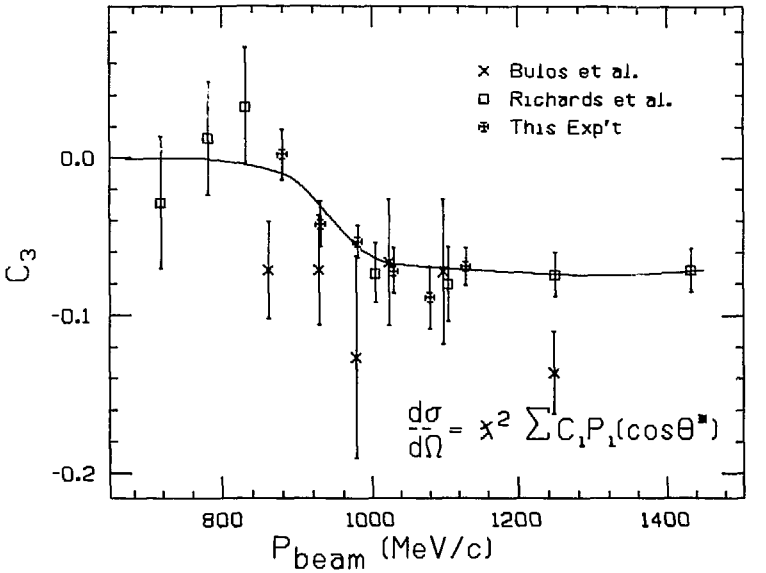

XBL 752-231

Figure 16f Legendre Coefficients

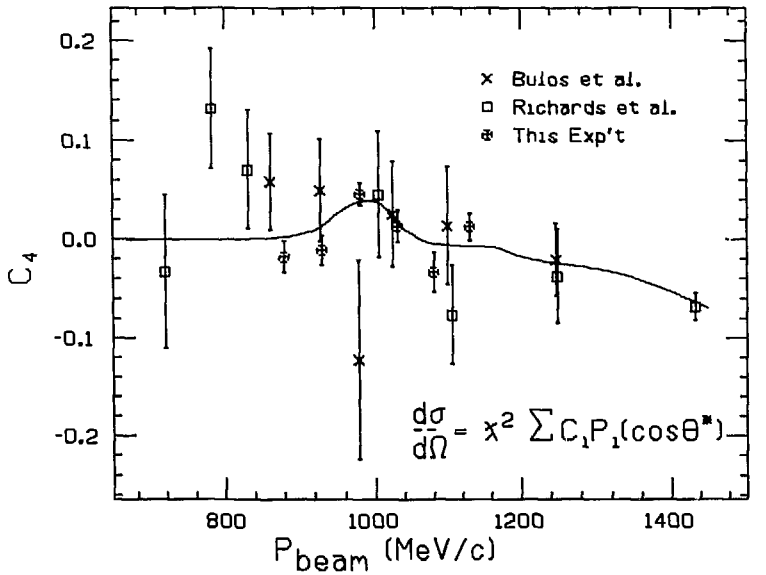

XBL 752 232

Figure 16g Legendre Coefficients

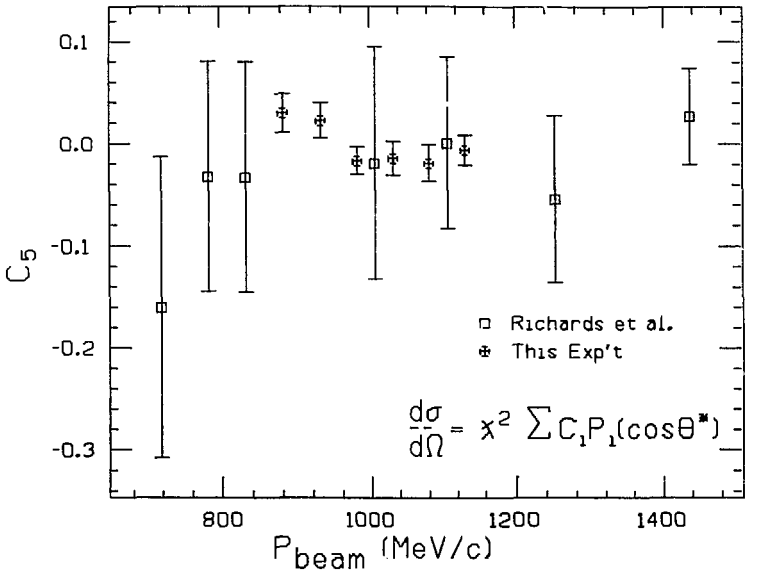

XBL 752-233

B. Interpretation

1. Individual Spin-Parity States in the Differential Cross-Section

It is possible to expand the initial and final states of reaction (1) as a sum of eigenstates of the constants of motion. In the case of strong interactions, both angular momentum and parity are conserved, and it is possible to examine the effects in this reaction of each state with definite angular momentum and parity. (Whether or not this is useful depends on how many states must be considered. As we have seen, only a limited number of Legendre polynomial terms are visible in this analysis.)

Ashkin[35] shows that if the reaction is represented by the equation

$$\Psi_f = M \Psi_i$$

where Ψ_i is the wavefunction for the initial state,

Ψ_f is the wavefunction for the final state,

and M is the transition matrix for the interaction, then general invariance arguments suffice to show that M must have the form

$$M = f + g\,\vec{\sigma}\cdot\vec{n}$$

where $\vec{n}$ is the normal to the plane of the interaction,

$\vec{\sigma}$ is the Pauli spin operator,

and f and g are functions of the incident and final state momentum vectors.

The differential cross-section is given by

$$\frac{d\sigma}{d\Omega} = |f|^2 + |g|^2 \qquad (5)$$

Expanding the incoming and outgoing wavefunctions as sums of terms, each of definite spain and parity, requires

$$f = \lambda \sum_{\ell} [(\ell+1)T_{\ell}^{+} + \ell T_{\ell}^{-}] P_{\ell}(\cos\theta) \qquad (6a)$$

$$g = i\lambda \sum_{\ell} [T_{\ell}^{+} - T_{\ell}^{-}] P_{\ell}^{1}(\cos\theta) \qquad (6b)$$

where $T_{\ell}^{\pm}$ corresponds to the amplitudes for $J = \ell \pm \frac{1}{2}$ and $P_{\ell}^{1}(\cos\theta) = \sin\theta \frac{d(P_{\ell}(\cos\theta))}{d(\cos\theta)}$ is the asscciated Legendre function.

Substituting equation (6) into equation (5) gives an expression in the squares of legendre polynomials and associated functions. Integrating over all angles gives

$$\sigma = 4\pi\lambda^2 \sum_{\ell} (\ell+1)|T_{\ell}^{+}|^2 + \ell|T_{\ell}^{-}|^2 = 4\pi\lambda^2 \sum (J+\tfrac{1}{2})|T|^2 \qquad (7)$$

With some algebra and bookkeeping, the expression for the differential cross-section can be reduced to a sum of Legendre polynomials, of higher order. Tripp[36] gives a useful table of coefficients, using the notation L_{2J}, so that $T_0^{+} = S_1$, $T_1^{-} = P_1$, $T_1^{+} = P_3$, $T_2^{-} = D_3$, etc. In this notation, and assuming complex conjugation, so that for each term AB one must use $Re(A^*B)$,

$$\frac{d\sigma}{d\Omega} = \lambda^2 [\ P_0(\cos\theta)[S_1S_1 + P_1P_1 + 2(P_3P_3 + D_3D_3) + 3(D_5D_5 + F_5F_5)]$$

$$+ P_1(\cos\theta)[2S_1P_1 + 4(S_1P_3 + P_1D_3) + (4/5)(P_3D_3) + (36/5)(P_3D_5 + D_3F_5) + (18/35)(D_5F_5)]$$

$$+ P_2(\cos\theta)[4(S_1D_3 + P_1P_3) + 6(S_1D_5 + P_1F_5) + 2(P_3P_3 + D_3D_3) + (12/7)(P_3F_5 + D_3D_5) + (24/7)(D_5D_5 + F_5F_5)]$$

$$+ P_3(\cos\theta)[6(S_1F_5 + P_1D_5) + (36/5)(P_1D_3) + (24/5)(P_3D_5 + D_3F_5) + (16/5)(D_3F_5)]$$

$$+ P_4(\cos\theta)[(72/7)(P_3F_5 + D_3D_5) + (18/7)(D_5D_5 + F_5F_5)]$$

$$+ P_5(\cos\theta)[(100/7)D_5F_5] \quad] \qquad (8)$$

I have left out terms containing amplitudes with spin greater than 5/2, since they would also require terms in higher order, which are not visible in the experimental data. This equation corresponds in form to previous fits to the experimental data of the form

$$\frac{d\sigma}{d\Omega} = \lambda^2 \sum_{\ell=0}^{5} C_\ell P_\ell(\cos\theta) \qquad (9)$$

Analysis of pion-nucleon elastic scattering and charge exchange data has shown a number of heavy baryon resonances with isospin 1/2, which could couple with the eta-neutron channel. The "well-established" resonances in Table X are listed in the Review of Particle Properties[3], which summarizes the results of numerous authors[3'], mainly, in this case, from partial-wave analyses. The existance of these resonances is of interest in the following discussion, although only the N(1535) is known to be strongly coupled to the eta-neutron channel.

Table X. "Well-Established" Resonances

Name	L_{2J}	Mass (MeV)
N(940)	P_1	939
N(1470)	P_1	1400 to 1470
N(1520)	D_3	1510 to 1540
N(1535)	S_1	1500 to 1600
N(1670)	D_5	1670 to 1685
N(1688)	F_5	1680 to 1690
N(1700)	S_1	1665 to 1765
N(1780)	P_1	1650 to 1860
N(1810)	P_3	1770 to 1860

One may choose from this table according to one's own taste, to explain the limited data in the eta-neutron channel. The selection is more than enough, because each state has a mass, a width, and coupling constants to both πN and ηn channels, all of which vary with the details of the fit being done. It is a long way from equation (8) to equation (9). The following section refers to these equations, and to the coefficients of equation (9) shown in Fig. 16.

2. Bump-Hunting in the Eta Data

The C_4 coefficient in the Legendre polynomial fits to the differential cross-section shows a peak at about 980 MeV/c (1660 MeV), with a size of 0.046 ± 0.011. It could be due to a resonance in either the F_5 or the D_5 wave. Either is possible, especially since resonances have been found in both waves by phase-shift analysis of pion-nucleon interactions, and the behavior of C_4 is by itself insufficient to distinguish them. The question could be resolved by an analysis of interference with other known resonances as seen in other coefficients, or by a measurement of polarization parameters, which are sensitive to the difference in parity between the F_5 and the D_5 waves. D_5 and F_5 are not both present, for their interference would produce a C_5 term, which is absent in the experimental results. The spin-5/2 terms appear in equation (8) with a coefficient (18/7), giving

$$|D_5|^2 \text{ or } |F_5|^2 = (7/18)(0.046 \pm 0.011) = 0.018 \pm 0.004$$

Inserting this value into equation (7) gives

$$\sigma = 4\pi\lambda^2(3)(|D_5|^2 \text{ or } |F_5|^2) = (0.84 \pm 0.21) \text{ mb}$$

This is the cross-section for $\pi^-p \rightarrow \eta n$ going through the spin-5/2 channel. Calculations[38] based on an SU(3) model predict a branching fraction of 2% into ηn for the $D_5(1670)$, giving

$$\sigma = (2/3)(0.4)(0.02)(J+\tfrac{1}{2})(4\pi\lambda^2) = 0.26 \text{ mb.}$$

(In this calculation, (2/3) is the fraction of the initial π^-p state which is pure isospin 1/2. The

factor 0.4 is the branching fraction of the intermediate state to the initial $\pi^- p$ state[3], and 0.02 is the branching fraction to ηn.) The same calculations give zero for the branching fraction into ηn for the F (1688) resonance. Thus, it seems likely that the observed interaction is $\pi^- p \rightarrow D_5(1670) \rightarrow \eta n$.

There is structure in C_1, C_2, and C_3 in this region as well. This could be due to interference terms between the D_5 (or F_5) and other waves which are present but not resonant at this energy. An $S_1 D_5$ term would affect the C_2 coefficient, a $P_1 D_5$ term would affect C_3, and an $S_1 P_1$ term would affect C_1. (Similarly, $S_1 F_5$ affects C_3 and $P_1 F_5$ affects C_2, so this is no direct help in separating the effects of D_5 and F_5).

The total cross-section, and more obviously the C_0 coefficient, show a minimum at 1000 MeV/c (1670 MeV), followed by a peak at 1200 MeV/c (1780 MeV). A dip in total cross-section cannot be explained by a resonance or by interfering resonances, so it is more attractive to interpret this as a peak at the higher energy. This could be due to the P_1 (1780) resonance which has been seen in πN phase-shift analysis.

ACKNOWLEDGEMENTS

Many people have contributed to the work described in this thesis. For instance, it could not have been done without the cooperation of the Bevatron crew and the L.B.L. computer staff. However, some individuals stand out.

My graduate advisor, Professor A. C. Helmholz, helped me through the Berkeley experience with good advice, willingly given.

Dr. R. W. Kenney helped and taught me during the experimental work, and made valuable suggestions concerning the thesis.

The other physicists and graduate students involved in the experiment have all shared with me their knowledge and their friendship. They are Orin Dahl, Ivan Linscott, Jerry Nelson, Morris Pripstein, Tom Risser, Andris Skuja, and Mike Wahlig. Each of these people has given me far more than I can acknowledge.

I am grateful to Bill Oliver, Sherwood Parker and Charles Rey for building the spark chamber system and teaching us how to run it.

I am grateful to Bob Hogrefe and the L.B.L. Group A scanning and measuring staff for scanning hundreds of thousands of frames of film, and to Ellen Epstein for maintaining the orderly flow of data in the analysis.

Mike Long built some of the experimental apparatus, and Tim Daly drew some of the figures used in this thesis. I thank them both.

Finally, I thank my wife Kelly, and my family, for their patience and understanding during the times when I was physically or mentally absent.

This work was done under the auspices of the U. S. Atomic Energy Commission.

REFERENCES

1. A. Pevsner, R. Kraemer, M. Nussbaum, C. Richardson, P. Schlein, R. Strand, T. Toohig, M. Block, A. Engler, R. Gessaroli, and C. Meltzer, P. R. L. 7, 421 (1961).

2. See, for example, G. Puppi, Ann. Rev. Nuc. Sci. 13, 287 (1963). for a description of the determination of the quantum numbers of the eta meson.

3. Values from the averages compiled by the Particle Data Group, in Rev. Mod. Phys. 45, No. 2, S1 (1973).

4. W. B. Richards, C. B. Chiu, R. D. Eandi, A. C. Helmholz, R. W. Kenney, B. J. Moyer, J. A. Poirier, R. J. Cence, V. Z. Peterson, N. K. Sehgal, and V. J. Stenger, P. R. L. 16, 1221 (1966).

5. P. Bulos, R. R. Lanou, A. E. Pifer, A. M. Shapiro, C. A. Bordner, A. F. Erenner, M. E. Law, R. R. Ronat, P. D. Rudnick, K. Strauch, J. J. Szymanski, P. Bastien, B. B. Bratson, Y. Eisenberg, B. T. Feld, V. K. Kistiakowsky, I. A. Pless, L. Rosenson, R. K. Yamamoto, G. Calvelli, P. Gasparini, L. Guerriero, G. A. Salandin, A. Tomasin, L. Ventura, C. Voci, and P. Waldner, Phys Rev. 187, 1827 (1969).

6. P. J. Litchfield, Phys. Rev. 183, 1152 (1969).

7. W. Deinet, H. Mueller, D. Schmitt and H.-M. Staudenmaier, Nuc. Phys. B11, 495 (1969).

8. W.H. Jones, D.M. Binnie, A. Duane, J.P. Horsey, D.C. Mason, J.A. Newth, I.U. Raman, J. Walters, N. Horwitz, P. Palit, Phys Letters 23, 597 (1966).

9. Y. Lemoigne, P. Granet, F. Marty, R. Ayed, P. Bareyre, P. Borgeaud, M. David, J. Ernwein, J. Feltesse and G. Villet, "The Reaction $\pi^- p \rightarrow \eta^0 n$ Up to $p = 400$ MeV/c: Experimental Results and Partial Wave Analysis." Proceedings of BARYON RESONANCES - 73, Purdue University, West Lafayette, Indiana (1973).

10. John C. Botke, Phys. Rev. 180, 1417 (1969).

11. S.R. Deans and J.W. Rooten, Phys. Rev. 185, 1797 (1969).

12. R. Carreras and A. Connachie, Nuc. Phys B16, 35 (1970).

13. Thomas Bard Risser, "Neutral Decays of the η^0 Meson", (Ph. D. Thesis) Lawrence Radiation Laboratory Report UCRL-20039 (1970) (unpublished).

14. BOPUS is descended from PCCOS, a program for the CDC 6600 by Elen Close (private communication). It uses Bevatron magnetic field measurements made by the L.R.L. Magnet Test Group, provided to me by Loren Meissner.

15. Thomas J. Devlin, "OPTIK: An IBM 709 Computer Program for the Optics of High-Energy Particle Beams", Lawrence Radiation Laboratory Report UCRL-9727 (1961) (unpublished).
Modified for the CDC-6600 by Arthur Greenburg.
Modified and expanded by Roger Chaffee.

16. Bruce Cork, Denis Keefe, and William A. Wenzel, Proc. of International Conf. on Instrumentation for High-Energy Physics p. 81. Interscience Publishers, New York (1961).

17. Risser, op. cit. p. 44.

18. ibid. pp. 119-130.

19. Richard J. Kurz, "A 7C9/7090 Fortran II Program to Compute the Neutron Detection Efficiency of Plastic Scintillator for Neutron Energies from 1 to 300 MeV", Lawrence Radiation Laboratory Report UCRL-11339 (1964) (unpublished)
Rewritten in FORTRAN IV for the CDC-6600 and IBM 360/91 by Roger Chaffee.

20. R. J. Cence, B. D. Jones, V. Z. Peterson, V. J. Stenger, J. Wilson, D. Cheng, B. C. Gandi, F. W. Kenney, I. Linscott, W. E. Oliver, S. Parker, and C. Rey, P. R. L. 22, 1210 (1969).

21. C. A. Rey and S. I. Parker, Nucl. Instr. Meth. 54, 314 (1967).
S. I. Parker and C. A. Rey, Nucl. Instr. Meth. 43, 361 (1966).

22. L.B. Robinson, F. Gin, and F.S. Goulding, "A High-Speed 4096-Channel Analogue-Digital Converter for Pulse-Height Analysis", Lawrence Radiation Laboratory Report UCRL 17419, January 1968 (unpublished).

23. C. O. Gieber, M. Leavitt, and F. Chaffee, L.R.L. Group A Programming Note P-194 (unpublished).

24. A. R. Clark and I. T. Kerth, Proceedings of the 1966 International Conference on Instrumentation for High Energy Physics, Stanford California (1966)

25. M. Leavitt and I. F. Linscott, L.R.L. Group A Programming Note P-188 (unpublished).

26. Max Leavitt, L.R.L. Group A Programming Note P-231 (unpublished).

27. Orin Dahl, L.R.L. Group A Programming Note P-221 (unpublished).

28. O. T. Dahl, T. R. Day, F. T. Solmitz, and N. L. Gould, L.R.L. Group A Programming Note P-126 (unpublished).

29. Jerome H. Friedman, "Random Event Generation with Nonconstant Frequency Distributions", Lawrence Radiation Laboratory Report UCRL 19206 (1969) (unpublished).

30. S.J. Linderbaum, Ann. Rev. Nuc. Sci. 11, 213 (1961).

31. Burton J. Moyer, private communication.

32. R.H. Dalitz, Proc. Phys. Soc.(London), A64, 667 (1951).

33. Jerry Nelson wrote the original version of "FCLLY" for the IBM computers. I have modified it and used it at SLAC.

34. Jerry Earl Nelson, "A High Statistics Study of the Reaction $\pi^- p \rightarrow \pi^0 n$ Between 1.0 and 2.4 GeV/c" (Ph.D. Thesis), Lawrence Berkeley Laboratory Report LBL-1019 (1972) (unpublished).

35. J. Ashkin, Suppl. Nuovo Cimento, 14, 221 (1959).

36. R. D. Tripp, "Baryon Resonances", CERN Report 65-7 (1965) (unpublished).

37. See, for instance, S. Almehed and C. Lovelace, Nucl. Phys. B40, 157 (1970).

38. D.E. Plane, P. Baillon, C. Bricman, M. Ferro-Luzzi, J. Meyer, F. Pagiola, W. Schmitz, E. Burkhardt, H. Filthuth, E. Kluge, H. Oberlack, F. Barloutaud, P. Granet, J.P. Porte and J. Prevost, Nuclear Physics B22 93 (1970).